Capillary-mediated interface perturbations: Deterministic pattern formation

Martin E. Glicksman

College of Engineering, Florida Institute of Technology, 150 West University Blvd., Melbourne, FL 32901-6975, USA

ABSTRACT

Leibniz–Reynolds analysis identifies a 4th-order capillary-mediated energy field that is responsible for shape changes observed during melting, and for interface speed perturbations during crystal growth. Field-theoretic principles also show that capillary-mediated energy distributions cancel over large length scales, but modulate the interface shape on smaller mesoscopic scales. Speed perturbations reverse direction at specific locations where they initiate inflection and branching on unstable interfaces, thereby enhancing pattern complexity. Simulations of pattern formation by several independent groups of investigators using a variety of numerical techniques confirm that shape changes during both melting and growth initiate at locations predicted from interface field theory. Finally, limit cycles occur as an interface and its capillary energy field co-evolve, leading to synchronized branching. Synchronous perturbations produce classical dendritic structures, whereas asynchronous perturbations observed in isotropic and weakly anisotropic systems lead to chaotic-looking patterns that remain nevertheless deterministic.

© 2016 The Author. Published by Elsevier B.V. This is an open access article under the CC BY-NC-ND license (http://creativecommons.org/licenses/by-nc-nd/4.0/).

1. Introduction

1.1. Background

Crystal–melt interfaces remain macroscopically featureless at full equilibrium, or when they grow or melt in a stable mode. When interfaces become morphologically unstable, however, they often evolve into complex forms comprised of dimples, ripples, cells, and dendrites, the temporal details of which are thought to be influenced by several factors. These include crystalline anisotropy; the presence of persistent interface-distorting defects, including intersecting phase boundaries, sub-boundaries, or terminating dislocations; disturbances initiated where contacts occur with container walls; and from the spectra of thermal and pressure fluctuations from intrinsic (thermodynamic) and extrinsic (environmental) sources.

Experiments and theoretical studies on maintaining stability to avoid interfacial 'breakdown', uncontrolled microstructures, and severe chemical microsegregation, concern subjects of considerable practical importance to crystal growers. Indeed, investigations into these subjects are ongoing for over six decades, following early 'decanting' experiments that first allowed optical viewing of solid–liquid patterns in metals and alloys [1,2]. The formation of decanted substructures was explained by stability conditions at the solid–liquid interface, using the criterion of 'constitutional supercooling', an

early theory of interface stability developed by B. Chalmers and his co-workers [3,4]. Constitutional supercooling became a precursor of modern morphological stability theories, for which up-to-date literature reviews may be found in [5,6], each covering related *in situ* experiments on interface control, numerical studies of interface evolution, and linear and non-linear dynamic analyses.

In their 2009 overview Asta et al. [7] underscored the importance of understanding the fundamental mechanisms of pattern evolution in solidification, crystal growth, and related solid-state transformations. In 2011, the author re-analyzed a NASA archive containing hundreds of carefully controlled microgravity crystal growth and melting data [8]. (Also see Ref. [9] for the online URLs providing public access to NASA microgravity data.) Experiments were successfully conducted aboard Space Shuttle *Columbia* with the Isothermal Dendritic Growth Experiment (IDGE). The IDGE provided a primary research experiment on three United States Microgravity Payload Missions (USMP-2, 3, and 4), which flew in low-Earth orbit during the mid-1990s [10–12]. Our re-analysis of those experiments [13] uncovered an initially overlooked, but remarkable, phenomenon captured on IDGE's video melting data, the main feature of which was observation of conduction-limited melting in microgravity with unexpected crystallite shape changes following self-similar melting. Conduction-limited melting with the occurrence of spontaneous shape change was studied recently using numerical simulations, with good correspondence found between the experiments and these simulations [14]. The conclusion reached was that capillarity was responsible, although an explicit mechanism was not identified.

A few implications concerning the kinetics of melting, based on reinterpretation of those IDGE data, were reported in reference [8]. Now, through additional studies, to be detailed herein, the unusual melting results first observed and recorded in USMP-4 are far better understood theoretically. This allows a thermodynamically-based theory to explain crystallite shape change during melting more fully and provides a new dynamical mechanism for the evolution of pattern complexity accompanying unstable crystal growth. The theory, as developed in this paper, also elucidates an unrecognized kinetic pathway by which crystal–melt systems approach equilibrium or reach constrained stationary states.

In brief, the microgravity experiments referenced above uniquely allowed high-precision measurements of melting kinetics for needle-shaped crystalline fragments of pivalic anhydride (PVA). Ultra-high purity (7–9 s) PVA, $(CH_3)_3CCOOH$, was cyclically melted, supercooled, nucleated, and partially crystallized into dendrites. The crystals were re-melted to allow the next growth sequence under low gravity, $10^{-7}g_0$, where $g_0 = 9.8$ m s^{-2}.

Prior to total melting, a few isolated crystallites remained perfectly suspended and motionless in the warmer melt, as they were progressively consumed by quasi-static melting. These crystallites were slender prolate ellipsoids of revolution, with major axes initially about 1–1.5 cm, initially exhibiting large, needle-like axial ratios, with $C/A \approx 15$. Microgravity suppresses hydrodynamic motions from sedimentation and thermal buoyancy forces, except for an extremely small, outward, advective flow from each crystallite due to the 1% density decrease accompanying melting. Although the author was familiar with interface shape changes in crystals induced by melt hydrodynamics [15–21], the shape changes observed during melting in microgravity were free of any substantial fluid mechanical interactions.

Analysis of the images recorded during melting in microgravity showed that the large axial ratios of these crystallites initially increased slowly as melting progressed, then remained constant upon further melting. However, about half way toward their total extinction as crystals, their large C/A ratios, as needle crystals, decreased by almost an order-of-magnitude to nearly unity. We observed, in other words, that the onset of dramatic shape change (needles melting into spheres) *always* began after the crystallite's initial centimeter-long C-axis decreased to about 5 mm, and its A-axis, or diameter, was correspondingly reduced to a few hundred micrometers. We reported that the axial ratios of isolated melting crystallites decreased from their initially high values toward unity, indicating that their acicular shapes spontaneously changed to spheroidal ones during active melting [22–24].

A quantitative comparison of theoretical melting rates and self-similar shape predictions was presented that was based on analytical and numerical analyses of quasi-static heat flow during melting in microgravity. We demonstrated mathematically that during melting the external heat conduction from the surrounding melt alone would actually keep constant the C/A ratios of isolated melting ellipsoids. Thus, the normal heat flow responsible for the melting transformation did not account for the observed spontaneous shape changes.

1.2. Approach

Crystal–melt interfacial tension was instead suggested as a possible cause for the reported profound shape changes prior to extinction from melting. An additional suggestion was offered, without proof, that the same mechanism responsible for shape changes during melting might also operate during crystal growth, and possibly self-stimulate pattern formation in a manner not recognized prior to these microgravity experiments. Some preliminary ideas based on the Le Chatelier–Braun effect [25,26] that relates curvature and shape changes to shifts in local interfacial

equilibrium were offered subsequently [27] to explain spontaneous shape modification during melting, and which might also influence interfacial patterns during crystallization.

The purpose of the present study is to show that capillary-mediated energy fields capable of interface shape modulation occur during *both* crystal melting and growth, and, in fact, are expected on fundamental thermodynamic and kinetic grounds. These capillary-mediated interface fields, moreover, are omnipresent during melting and growth under local equilibrium. Also, depending on feature size, these fields can perturb the motion of the interface during transformation and modulate its shape. Self-induced perturbations, moreover, stimulate pattern evolution, and promote the formation of complex phase arrangements associated with dendritic crystals and seaweed-like forms that are commonly observed in some alloy microstructures.

The energy fields to be described here *always* entail at least one of *two* basic forms of interfacial variation usually present on crystal–melt interfaces: (1) geometric shape variation, i.e., any non-uniform distribution of curvature with interface position and orientation; and (2) anisotropy of the interfacial energy density caused by directional dependence of underlying crystalline molecular fields. Indeed, even between fluids, all non-circular interface shapes in 2-D, or non-spherical shapes in 3-D, always exhibit the first, i.e., shape, or curvature variations, whereas crystal–melt interfaces also support energy anisotropy. Autogenous perturbations that develop during crystal growth or melting derive from these intrinsic interfacial variations are described in detail later. Examples to be presented demonstrate how one or both types of interfacial variation directly control shape changes and stimulate the formation of complex interface patterns.

Many forms of natural and industrial crystal growth and solidification occur under local thermodynamic equilibrium. It is, however, an interface's dynamical approach, along with local equilibrium that causes autogenous interfacial perturbations. We begin with a discussion of interfacial equilibria in its various forms, show the origin of the important capillary-mediated fields, and then compare our analytical field theory with results derived through dynamic numerical simulations.

2. Global and local equilibria

2.1. Global equilibrium

A crystal–melt system achieves the state of global thermodynamic equilibrium when its enclosing interface is everywhere at rest, and the crystal, at fixed volume, assumes its unique, stationary, Wulff configuration at minimum free energy [28]. Attainment of global equilibrium in solids generally requires an exceedingly long time, even for relatively small crystals, as global equilibrium involves *all* the atoms of a heterogeneous system. The equilibrium Wulff shape for such systems occurs at constant volume if, and only if, the crystal's chemical potentials are everywhere uniform, and all macro-gradients vanish both within the bulk phases and on their common interfaces and exterior surfaces.

By contrast, crystal growth, and phase transformation in general, are non-equilibrium processes that require the presence of robust thermal and concentration gradients to transport energy and matter, respectively, over macroscopic distances. Such macro-gradients weaken over time as growth slows and equilibrium is approached, and eventually vanish as free energy is fully extracted from the metastable melt phase. No further macroscopic changes occur in heterogeneous systems at full thermodynamic equilibrium.

2.2. Local equilibria and convexity

Shape changes induced through melting and crystal growth, and pattern evolution on growing unstable interfaces—both non-equilibrium processes—are the subjects of interest here. Shape changes and pattern evolution can develop as an interface departs imperceptibly from a state of 'local' equilibrium. In fact, despite the occurrence of free energy dissipation within the bulk phases during melting or freezing, local equilibria on active interfaces requires only that temperature, pressure, and the chemical potentials of each phase match across their common interface. Point-wise matchings of pressure and chemical potentials on heterogeneous phases occur rapidly through microscopic interactions among relatively few neighboring molecules or atoms surrounding the interface. This near-instantaneous equilibration between phases contrasts with the lengthy process of establishing macro-gradients that transport energy and diffuse matter over long distances, allowing advancement of the phase transformation. Such transport involves tens of millions of atoms or molecules through the surrounding bulk phases. Despite free energy dissipation and entropy production *within* the bulk phases, a heterophase system's microscopically thin interface often can evolve rapidly, yet remain essentially at local equilibrium.

We choose for the analysis developed here in two-dimensions (2-D) an initially smooth, at least twice differentiable, crystal–melt interface shape, designated $c(x, y) = 0$, $(x, y) \in \mathbb{R}^2$, for which the instantaneous in-plane curvature, $\kappa(x)$, is calculable at all points. It proves to be convenient mathematically to re-cast the Cartesian interface shape, $c(x, y) = 0$, which may be open or closed on the x–y plane, as a planar trace, or curve, designated $c(s(\varphi)) = 0$. Then, its interfacial arc length, $s(\varphi)$ {φ: $[0, 2\pi] \to \mathfrak{R}$}, where φ is the normal angle and $\mathfrak{R}$ is the set of all points on $c(x, y) = 0$. The normal angle along $s(\varphi)$ tracks the interface's local orientation and instantaneous shape, which is related to the corresponding slope angle, $\theta \equiv \tan^{-1}(\frac{dy}{dx})$, by the complementary relationship $\varphi = \theta - \frac{\pi}{2}$. The interface shapes to be analyzed in 2-D are kept sufficiently simple, precluding such complications as highly convoluted interfaces or where an interface turns back on itself. The required thermodynamic and geometric functions of φ, and the profile itself, remain everywhere single-valued for all the shapes treated analytically in this study. Where interfaces might eventually become topologically challenging, such as occurs in numerical models, then arc length parameterization becomes necessary. Fig. 1 displays such an arbitrary smooth solid–liquid interface, along with its Cartesian coordinates and the interface's local unit normal, $\mathbf{n}(\varphi)$, and tangent vector, $\tau(\varphi)$.

The instantaneous values of chemical potential, its gradient and tangential energy flux, and, ultimately, the surface divergence of that flux, will all be determined *analytically*, based on the instantaneous shape and arc length of the initial interface, and the selected symmetry and anisotropy of the surface energy density function, $\gamma(\varphi)$. Consequently, we limit the current discussion to single-component, two-phase systems, so that the solid–liquid interface has balanced normal stresses, and maintains equilibrated solid- and liquid-phase chemical potentials (i.e., matched temperatures and pressure) from point-to-point along that interface. These conditions are necessary to specify local equilibrium prevailing on an interphase interface in a unary system, and are equivalent to matching the local equilibrium temperature of the crystal, c, with its liquid phase, ℓ, i.e., $T_c(\varphi) = T_\ell(\varphi)$. The condition of matched thermo-potentials can be closely approximated during crystal growth, provided that: (1) the interface speed remains moderate, and (2) that kinetic interference to molecular attachment/detachment at the interface is negligible.

The latter requirement favors so-called 'atomically rough' interfaces, devoid of equilibrium facets or other kinetic hindrances.
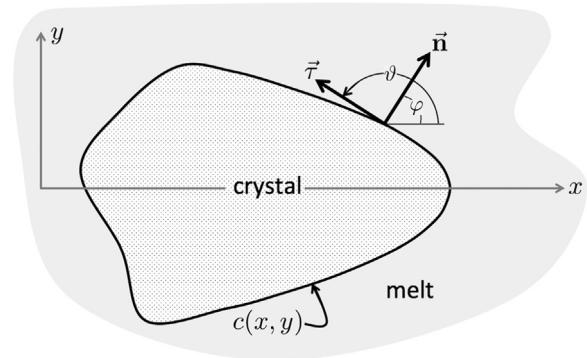

Fig. 1. 2-D crystal–melt interface, $c(x, y) = 0$. The interfacial arc length, $s(x, y)$, and the normal angle, $\varphi(s)$, changes smoothly from any arbitrary point on the interface when moving in the $+_\tau$ tangential direction, traveling anti-clockwise round the crystal–melt interface, with the crystalline phase on the left. In turn, both the local normal angle, φ, and the slope angle, $\theta = \varphi + \frac{\pi}{2}$, each increase by 2π after a complete circuit of the interface. The interface curvature is chosen as positive over the convex portions of the boundary, with the unit normal vector, $\mathbf{n}$, always pointing outward into the surrounding melt. Subsequent melting or growth of the crystal depend on the temperature of the melt phase far from the interface, relative to the system's melting temperature, T_m.

Interfacial facets represent energetically suppressed, i.e., 'missing', interface orientations, where discontinuous jumps appear in the distribution of normals along the interface. Avoiding facet formation under local equilibrium imposes limits on the strength of the energy density anisotropy, as set by lattice symmetry. This restriction stipulates convexity of the energy density over all crystallographic orientations ($0 \le \varphi \le 2\pi$). A so-called convex polar γ-plot for a crystal–melt interface simplifies the ensuing analysis of capillary-mediated energy fields by eliminating jumps in the normal and tangential vectors. This restriction insures that the interface curvature function remains everywhere smooth, continuous, and at least twice differentiable.

3. Interface potential

The thermodynamics of interfaces has been studied in impressive detail, with earlier investigators identifying all the forms of energy release and storage that can be associated with translating, rotating, or otherwise altering the position, orientation, or shape of interfaces [29,30]. What remains incomplete, however, is how these energy rates link with interfacial dynamics, and extend our understanding and grasp of kinetically complex phenomena, including evolution, prediction, and control of diffusion- and conduction-limited patterns. Indeed, to the author's knowledge, detailed quantitative dynamics of how capillary-mediated thermodynamic fields produce microstructure patterns has not been formulated previously.

The most general thermodynamic relationship that supports the constraint of local interfacial equilibrium between two bulk phases is the Gibbs–Thomson–Herring (GTH) condition [31–33]. The GTH condition derives from the Euler–Lagrange variational equation [34,35] that minimizes the excess free energy of a smooth interface with changing curvature over its arc length (i.e., what we term as 'shape variation') and with local energy densities that vary with orientation (i.e., energy anisotropy). This interface continually matches the thermo-chemical potentials of both phases to satisfy the requirement of local equilibrium. Application of the GTH interface condition to a unary system that undergoes melting or freezing at local equilibrium is tantamount to achieving a point-wise match of the curvature-dependent temperature distributions between adjacent phases. With uniform external pressure exerted over the interface, the application of *local* equilibrium

extends classical thermostatic equilibrium to curved interfaces evolving dynamically during phase transformation.

3.1. Gibbs–Thomson–Herring (GTH) distribution

Local equilibrium established along the arc length, s, of a two-dimensional curved interface, $c(\varphi(s)) = 0$, depends both on the in-plane curvature, $\kappa(\varphi(s))$, and the anisotropic energy density specified by the energy density function, $\gamma(\varphi(s))$. The GTH temperature distribution thus always depends on the instantaneous *shape* of the solid–liquid interface and, if energetically anisotropic, on its crystallographic *orientation*, as specified by the interface's local normal vector field, $\mathbf{n}(\varphi)$ and the crystal's axes.

At the advancing front of such an anisotropic crystal, we set $x = y = \varphi = 0$, so that the normal vector, $\mathbf{n}(\varphi)$ at $\varphi = 0$, shown in Fig. 1, is parallel to one of the crystal's easy growth directions, say $\langle 10 \rangle$, which direction arbitrarily is also set parallel to the Cartesian $+x$ axis. The choices of crystal symmetry axes and interface coordinates specify the other easy growth orientations along with the corresponding polar form of the energy density anisotropy. In 2-D, for example, the maximum energy density directions for 4-fold harmonic symmetry are given by the energy density function $\gamma(\varphi) = \gamma_0(1 + \epsilon_4 \cos 4\varphi)$, the maxima of which have normal angles ($\varphi = 0, \frac{\pi}{2}, \pi, \frac{3\pi}{2}$) that align with the growth directions and the Cartesian axes.

These coordinate and crystallographic alignments specify that the equilibrium GTH temperature distribution on any 2-D interface arc-length position, s, and orientation, φ, is given by[1] [31]

$$T_{int}(\varphi) = T_m - \frac{T_m \gamma_0 \Omega}{\Delta H_f} \left(\frac{\gamma(\varphi(s)) + \gamma_{\varphi,\varphi}}{\gamma_0} \right) \kappa(\varphi(s)). \tag{1}$$

The melting temperature, T_m, appearing on the right-hand side of Eq. (1), is the equilibrium temperature of a stationary planar crystal–melt interface at the identical melt pressure; ΔH_f is the molar heat of fusion; Ω is the system's molar volume; and $\gamma_{\varphi,\varphi}$ denotes the second angular derivative of the orientation-dependent interfacial energy density, $\gamma(\varphi(s))$. The angular average of $\gamma(\varphi(s))$ over all orientations ($0 \leq \varphi < 2\pi$) defines the 'modulus' of the interfacial energy density, designated γ_0—a material constant that sets the magnitude of the interface energy density [J m^{-2}]. The in-plane curvature, $\kappa(\varphi(s))$ [m^{-1}], is defined arbitrarily to be positive where the interface is convex to the melt, and where local normals always point away from the crystal into its surrounding melt.

Slight rearrangement of Eq. (1) specifies the dimensionless GTH thermo-potential, $\vartheta(\varphi(s))$. The scalar field $\vartheta(\varphi(s))$ is the potential established along a curved interface with arbitrary shape $c(\varphi(s)) = 0$, for a two-phase unary system evolving at local equilibrium.

$$\vartheta(\varphi(s)) \equiv \frac{T_{int}(\varphi(s)) - T_m}{T_m} = -\frac{\lambda_c}{a} \left(\frac{\gamma(\varphi(s)) + \gamma_{\varphi,\varphi}}{\gamma_0} \right) \hat{\kappa}(\varphi(s)). \tag{2}$$

Here the ratio on the right-hand side of Eq. (2) is $\frac{\lambda_c}{a} = \frac{\gamma_0 \Omega}{a \Delta H_f} \ll 1$. This ratio defines the system's capillary constant, and allows introduction in Eq. (2) of the dimensionless interface curvature, $\hat{\kappa}(\varphi(s)) \equiv a\kappa(\varphi(s))$. The length scale, a [m], must be inserted to establish the crystal's feature size and scale the magnitude of its thermo-potential, $\vartheta(\varphi(s))$. The zeros of this potential occur where

the interface is flat, i.e., at locations where the interface temperature equals the melting point, $T_{int} = T_m$, and where $\hat{\kappa}(\varphi(s)) = 0 = \vartheta(\varphi(s))$. If capillarity itself were non-existent, then the GTH potential field vanishes. Whether a crystal melts or grows subsequently is determined, of course, by the temperature of the surrounding liquid phase relative to T_m.

3.2. Interface gradients

Local equilibrium, as formulated in Section 2.2, implies an active presence of the capillary-mediated GTH potential distribution during crystal growth or melting. This same specification, *without additional assumptions*, suggests the presence of potential gradients along an arbitrary curved interface. For example, in 2-D the temperature gradient along an interface $c(\varphi(s): x, y) = 0$ is found by multiplying the dimensionless thermo-potential, Eq. (2), by T_m, and then evaluating its tangential, or arc-length, derivative $\frac{d}{ds}(\vartheta(\varphi) \times T_m)$. That tangential derivative is found conveniently by applying the chain rule of differentiation

$$\frac{dT_{int}}{ds} = \frac{dT_{int}}{d\varphi} \left(\frac{d\varphi}{ds} \right) = \frac{d}{d\varphi} \left[\vartheta(\varphi) \times \frac{T_m}{a} \right] \hat{\kappa}(\varphi). \tag{3}$$

The explicit parametric notations used thus far to indicate that the normal angle is dependent on arc length, $\varphi(s)$, will be dropped henceforth to simplify the notation. Interface shapes and their higher derivatives that are selected for analysis in this article will be chosen as single-valued with respect to the normal angle variable, φ.

Accepting the GTH potential as a real interface thermodynamic field—not just as a boundary condition to link curvature and temperature—one finds in 2-D a capillary-mediated tangential gradient field established along the crystal–melt interface,

$$\mathbf{G}_\tau(\varphi) = \frac{\lambda_c T_m}{a^2} \left[\left(\frac{\gamma(\varphi)}{\gamma_0} \right) \hat{\kappa}(\varphi) \hat{\kappa}_\varphi + \left(\frac{\gamma_{\varphi,\varphi}}{\gamma_0} \right) \hat{\kappa}(\varphi) \hat{\kappa}_\varphi + \left(\frac{\gamma_\varphi + \gamma_{\varphi,\varphi,\varphi}}{\gamma_0} \right) \hat{\kappa}^2(\varphi) \right] \tau, \tag{4}$$

where τ is the dimensionless unit tangential vector along such an interface. See again Fig. 1.

The thermo-capillary gradient in 2-D consists of three terms: (1) The first term within the square bracket of Eq. (4) results solely from the shape, and contributes to the gradient field even if the interfacial energy density, $\gamma(\varphi)$, is a constant and the system lacks energy anisotropy[2]; (2) the second term arises from 'mixed' effects, that is where the shape of the interface (its curvature distribution) and its energy density *both* vary with position or orientation; and (3) the last term contributes to the potential gradient when anisotropic surface energy is imposed on interfaces having constant curvature, such as along circular interfaces in 2-D, or over spherical interfaces in 3-D. Thus, *any* crystal shape undergoing melting or growth supports some level of capillary-mediated tangential thermal gradients. It is the crystal's size factor, specifically, $1/a^2$, that establishes the actual magnitude of its vector gradients. Moreover, the only crystalline shapes exempt from the presence of capillary-induced thermal gradients are (equilibrium) Wulff shapes, for which *all* gradients and fluxes vanish. We note in passing that every term in Eq. (4) contributing to the tangential gradient field is extremely sensitive to subsequent changes in the interface shape imposed by growth, melting, or shape relaxation toward equilibrium. The presence of such thermodynamic gradient fields is ubiquitous.

---

[1] In three dimensions a sharp interface, $S(x, y, z, t) = 0$, may be described by compact surface 'patches' embedded in $\mathbb{R}^3$ [52]. The GTH temperature distribution in 3-D, in turn, can be specified, as does Eq. (1) for 2-D, by inserting a patch's mean curvature, $\mathcal{H}(\eta, \xi) = \frac{1}{2} \operatorname{Tr}\{\kappa_i\}$, where (ξ, η) are local surface coordinates, and κ_i ($i = 1, 2$) are the two principal curvatures on an interface patch. In 3-D, interface potential therefore depends on *two* angular derivatives of $\kappa_i(\eta, \xi)$ and $\gamma(\eta, \xi)$ [36].

[2] This term has particular relevance to pattern formation in fluid–fluid phase separating systems that lack energy anisotropy, and in crystal–melt systems displaying extremely weak energy density anisotropy.

3.3. Tangential energy fluxes

As just argued, crystals melting or growing under local equilibrium support shape- and size-sensitive capillary-mediated thermal gradients. One may argue further that such interfaces, although only several molecules thick, are manifestly capable of supporting the passage of a superficial flux of energy. The specific form of this energy flux is determined physically by the electronic properties of the adjacent phases. For example, the interfacial energy flux from the GTH gradient might consist of surface phonons in the case of non-electrically conductive phases, or perhaps represent a superficial current of free electrons where metallic or semiconducting phases are in contact. Irrespective of the exact nature of the physical entities that comprise the flux and carry energy and or mass along the interface, or even the microscopic structure of the interface itself, a *non-zero* interfacial thermal conductivity, K_{int}, will exist. Even in the strict continuum limit of an interface of 'zero' thickness, the GTH potential gradient nonetheless stimulates either on, or 'between', the bulk phases the passage of a *superficial* energy flux. This is the likely reason why thermodynamically consistent numerical models, to be discussed later, need absolutely no adjustment to accommodate superficial energy or species transport caused by the capillary-mediated field.

One finds, moreover, that the physical units borne by the thermal conductivity of an interface, K_{int}, are [W/K], in distinction to those units for conventional bulk-phase thermal conductivities that are [W/m K]. Superficial transport of heat, as postulated here, along geometrically varying or energetically anisotropic interfaces appears as the energetic analog to surface, or interfacial species diffusion. Indeed, the diffusivities of surface species on many kinds of surfaces and interfaces are already well-established material transport coefficients, measured experimentally, and abundantly reported for grain boundaries, interphase interfaces, and even for the exterior surfaces of materials [37–39]. Values for K_{int}—the 'thermal analog' of surface species diffusivities—remain, curiously, virtually unknown at present, as the general influence of minute tangential energy currents traveling along interfaces apparently has not been accorded much study. Superficial energy flows, as will be shown, however, prove to have dominant influences on many crystal growth and melting processes, and perhaps as well on other first-order diffusion-limited phase transformations.

The corresponding tangential energy flux, $\mathbf{\Phi}_\tau(\varphi)$, stimulated by the capillary gradient field of the GTH temperature distribution bears physical units of [W/m]. The instantaneous tangential interfacial heat flux may be found by applying the superficial form of Fourier's law of heat conduction [40], namely

$$\mathbf{\Phi}_\tau(\varphi) = -K_{int}\mathbf{G}_\tau(\varphi). \tag{5}$$

Introducing the expression for the tangential thermal gradient, $\mathbf{G}_\tau(\varphi)$, Eq. (4), into Fourier's law, Eq. (5), yields, after some algebraic rearrangement, the general expression in 2-D for capillary-mediated tangential energy flux

$$\mathbf{\Phi}_\tau(\varphi) = -\frac{K_{int}\gamma_0\Omega}{a^2\Delta S_f}\left[\left(\frac{\gamma(\varphi)+\gamma_{\varphi,\varphi}}{\gamma_0}\right)\hat{\kappa}(\varphi)\hat{\kappa}_\varphi + \left(\frac{\gamma_\varphi+\gamma_{\varphi,\varphi,\varphi}}{\gamma_0}\right)\hat{\kappa}^2(\varphi)\right]\boldsymbol{\tau}. \tag{6}$$

where Eq. (6) introduces the molar entropy of fusion, $\Delta S_f = \Delta H_f/T_m$ [J/mol K], and shows explicitly that the tangential energy flux strengthens rapidly with decreasing feature size, as a^{-2}.

We now explore the implications of capillary-mediated interfacial energy transport.

3.4. Transformation rates

It has been argued correctly, and quite generally, that a vector flux must possess a component acting in the direction of its interface motion in order to contribute net energy or matter during phase transformation. Capillary-mediated *tangential* fluxes, as a consequence of this logic, are, ostensibly, precluded from affecting phase transformations rates [41]. Indeed, this widely-held view has, in the opinion of the author, led to exclusion of tangential fluxes from energy/mass balances at active interfaces [42,43].

A pivotal point, apparently overlooked in conventional continuum energy balance arguments, but expressly explored in this study, is that although flux divergences must themselves uniformly vanish at all points *within* bulk phases participating in quasi-static transformations—a behavior fully consistent with Laplace's equation—the *superficial divergence* of the tangential interface flux, nevertheless, is not similarly constrained! Moreover, by applying rigorous energy conservation principles we shall prove that the superficial divergence of the tangential flux provides a locally varying (both positive and negative) scalar energy field. Consequently, this thermodynamic field provides both sources and sinks of energy along an active interface. Moreover, we prove that the superficial divergence of the tangential flux (as the flux itself is a 'conservative' vector field) is net-zero over closed interfaces. This net-zero property doubtless has also added to a prevailing misunderstanding concerning these issues. We next show that tangential flux divergences *must* be included in *mesoscopic* interface energy balances. Their inclusion, as to be demonstrated, accounts for the appearance of intrinsic speed perturbations on the interface, leading to shape modulations that amplify into patterns.

Two essential features of this thermodynamic field worthy of repetition at this point are: (1) the surface divergence of capillary-mediated tangential fluxes is non-zero almost everywhere, and (2) the surface divergence of this flux averages to zero over a closed interface. These peculiar fundamental properties of the capillary energy field combine to provide a clear distinction between familiar, uniformly-zero flux divergences everywhere *within* participating bulk phases (so-called Laplacian behavior), and apparently unrecognized non-zero local divergences of capillary fluxes along evolving interfaces.

In short, we find that the capillary-mediated GTH potential stimulates an energy flux lacking a component normal to the interface. Through the non-zero divergence of its vector gradient, this thermodynamic field interacts locally with the evolving interface. More importantly, the divergence of the tangential flux provides *autogenous* perturbations that modulate the dynamics of the interface, which leads to pattern formation.

The balance of this paper is devoted to demonstrating that capillary-mediated fluxes provide self-induced disturbances capable not only of modifying the shapes of stable (melting) crystals, but inducing complex patterns on unstable (growing) crystals. Although this energy field does not influence the *overall* rate, or total extent, of diffusion-limited phase transformations, its presence deterministically guides initial pattern-formation, and dominates the character and form of an interface's temporal and spatial behavior independent of environmental noise.

The existence, properties, and dynamical effects of capillary-mediated interfacial fluxes are discussed and developed mathematically from basic principles in the next several sections. That the surface-averaged flux and its divergence are both zero will also be proven. These facts underscore precisely how interfacial fields play an active role in dynamic pattern evolution. Prior to completing mathematical expressions for such fields in 2-D, based on Eq. (6), a general proof will be developed that demonstrates the existence of autogenous interfacial energy fields in both 3-D and 2-D. Specifically, component energy rates present on evolving interfaces in 3-D are tracked in detail by applying classic conservation principles via the Leibniz–Reynolds theorem [44,45].

4. Interfacial energy conservation

4.1. Two-phase local equilibrium, 3-D

We define a time-dependent bi-phase domain, $\mathcal{D}(t)$ in $\mathbb{R}^3$. This domain consists of an enclosing outer boundary, $\partial\mathcal{D}(t)$, with unit normals, $\mathbf{N}$, surrounding two contacting sub-volumes of pure (one component) crystal, $V_c(t)$, and pure melt, $V_\ell(t)$, separated by a sharp interface (see Fig. 2). This interface is a curved sub-area, $S(t)$, with independent unit normals, $\mathbf{n}$. This composite domain is subject to internal and external energy exchanges as the transformations of melting and/or crystal growth proceed at a solid–liquid interface $F(x, y, z, t) = 0$ embedded in $\mathbb{R}^3$.

Melting or crystallization are limited here to rates not exceeding those compatible with maintaining *local* thermodynamic equilibrium. Steep gradients normal to the solid–liquid interface develop within the solid and liquid phase sub-volumes, through which the latent heat of transformation is transported to, or from, the moving interface. These net energy rate changes are coupled to energetic exchanges with the environment. Local equilibrium, requiring point-to-point matching of temperature, normal stress, and chemical potentials over the sub-interface, $S(t)$, persists everywhere, as already outlined in Section 2.2.

Mathematical procedures needed to capture general conditions required for energy conservation on interfaces evolving at local equilibrium are similar to those already discussed by Lin and Segel and by Spencer et al. [46,47], of which the latter investigators formulated species conservation on solid–vapor interfaces subjected to surface diffusion [48,49]. We note for completeness that solid-state de-wetting provides yet another closely related phenomenon that leads to complex morphological changes induced by surface forces [50,51].

4.2. Transformation model

The bi-phase domain defined in Section 4.1, and depicted in Fig. 2, consists of contiguous regions of crystal, c, and melt, ℓ, with unit normal vectors, $\mathbf{N}$, that orient the exterior boundaries of each

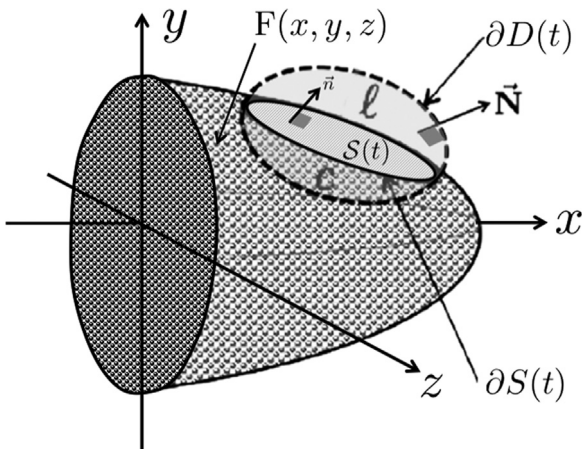**Fig. 2.** A crystalline interface, $F(x, y, z, t) = 0$, growing into its melt, from which a bi-phase domain, $D(t)$, samples a portion of each phase and the solid–liquid sub-interface area, $S(t)$, between them. Energy exchanges within and external to $D(t)$ are tracked via Reynolds's theorem. The domain consists of adjacent sub-volumes of melt, ℓ, and crystal, c, enclosed by an outer bounding surface, $\partial D(t)$, shown here as the dashed envelope, with its representative external unit normal, $\mathbf{N}$, pointing outward toward the surrounding phases. Sub-volumes within $D(t)$ are separated by the sub-area, $S(t)$, itself oriented by an independent set of internal normal vectors, $\mathbf{n}$, which point away from the crystal into the melt. The border of $S(t)$ in 3-D is a closed space curve, $\partial S(t)$, given by the intersection $F(x, y, z, t) = 0 \cap \partial D(t)$.

phase. The sub-volumes can mutually transform at their common sub-interface, $S(t)$, which is the internal boundary that divides the domain. This interior sub-interface has independent unit normal vectors, $\mathbf{n}$, pointing from the solid to the liquid, that define its orientation with respect to the crystal axes at each interfacial point, $\mathbf{r}(\eta, \xi, t)$, via local surface coordinates, (η, ξ), on the solid–liquid interface, and time, t.

The sub-interface within the domain, $S(t)$, is itself a compact surface, with smooth and continuous mean curvature, defined as $\mathcal{H}(\mathbf{r}) \equiv \frac{1}{2}\text{Tr}\{\kappa_{ij}\}$ [52]. The diagonal elements of the sub-interface's 2×2 curvature matrix are its principal curvatures, κ_{11} and κ_{22}. Where the solid and liquid phases touch, they share identical normal stresses and temperatures, $T_{int}(\mathbf{r})$, as specified by the GTH condition. The phases remain in *local* equilibrium at the uniform pressure established throughout the static melt. The interface evolves in 3-D with a continuous velocity field, $\mathbf{v}(\mathbf{r})$, causing absorption or release of latent heat into the surrounding phases at rates proportional to its local normal speed, $\mathbf{v}(\mathbf{r})\cdot\mathbf{n}$.

The volumetric enthalpy densities of the bulk phases constituting $D(t)$ are $H_c(\mathbf{R}_c, t)$ and $H_\ell(\mathbf{R}_\ell, t)$, respectively, where $\mathbf{R}_c$ and $\mathbf{R}_\ell$ are vectors denoting points within the sub-volumes of the crystalline and melt phase, respectively. Excess free energy is stored along the evolving sub-interface at a superficial density $\gamma(\mathbf{n})$, which can vary anisotropically with the crystallographic orientation of the interface, $\mathbf{n}$.

4.3. Energy conservation

The Reynolds theorem, in accord with the first law of thermodynamics, states that the total energy of this bi-phase domain, including its internal exchanges of heat and work[3] between the domain's outer and internal boundaries, less any losses of heat and work, remains constant over time.

That statement of energy conservation is expressed here through (Leibniz) time derivatives of volumetric and areal energies within the domain that balance energy exchanges with its environment. The Reynolds balance includes *all* rates of energy release, storage, and exchange. These energetic release and storage rates are expressed as total time derivatives within $D(t)$—appearing on the left-hand side of Eq. (7)—of solid- and liquid-phase volumetric enthalpies, $H_i(\mathbf{R}_i, t)$, plus the area-weighted interfacial energy density, $\gamma(\mathbf{n})$, on the sub-interface area, $S(t)$. The energy exchange rates to the environment also appear as integrals on the right-hand side of the Reynold's balance, Eq. (7).

The Leibniz–Reynolds transport theorem expresses the temporal energy balance

$$\frac{d}{dt}\left[\iiint_{\mathcal{D}(t)} H_i(\mathbf{R}_i, t)\, dV_i + \iint_{S(t)} \gamma(\mathbf{n})\, dA\right]$$
$$= \iint_{\partial\mathcal{D}(t)} \left(\frac{\mathbf{J}_i\cdot\mathbf{N}}{H_i(\mathbf{R}_i, t)}\right) H_i(\mathbf{R}_i, t)\, dA$$
$$+ \oint_{\partial S(t)} \mathbf{\Phi}_\tau(\mathbf{r})\cdot\sigma\, d\Sigma, \quad (i = c, \ell), \tag{7}$$

where the double integral on the right-hand side contains the energy exchange rates, $\mathbf{J}_i\cdot\mathbf{N}$, that account for components of fluxes exiting normal to the domain's outer boundaries, $\partial(D(t))$. These rates are measured with respect to a coordinate system fixed to the volume centroid of $D(t)$. The ratios $\mathbf{J}_i\cdot\mathbf{N}/H_i(\mathbf{R}_i, t)$ (produced in

---

[3] Pressure–volume exchange rates, kinetic energy, advective fluid flows caused by density differences, or influences from external fields such as gravity are ignored for the present purposes, but the reversible work (actually power) of interface stretching, and any energy storage or release by the phase transformation are included.

Eq. (7) by multiplying and dividing by the phase enthalpies, $H_i(\mathbf{R}_i, t)$, within the area integral) equal the local time-dependent normal speeds of the outer phase boundaries of the ith phase ($i = c, \ell$) relative to the domain's volume centroid. Those normal boundary speeds, when integrated over the external *areas* of each phase, actually calculate the *volumetric* enthalpies of the crystal and melt phases over time.

The line integral which follows on the right-hand side of Eq. (7) measures any energy leaving or entering through the border, $\partial S(t)$, of the solid–liquid sub-interface, $S(t)$. The integrand of this line integral, $\mathbf{\Phi}_\tau(\mathbf{r})\cdot\boldsymbol{\sigma}$, is the component of any superficial (tangential) fluxes that pass through the sub-area's border, located at $\mathbf{r} \in \partial S(t)$. That border, as labeled in Fig. 2, forms a closed space curve for interfaces in 3-D, which is defined as the intersection $\partial \mathcal{D}(t) \cap (F(x, y, z, t) = 0)$. The sub-interface itself forms the so-called 'capping surface' to its border, which is the surrounding space curve. The space curve, $\partial S(t)$, consists mathematically of continuously oriented, infinitesimal line elements, $(d\Sigma)\mathbf{u}$, where $\mathbf{u}$ is a second unit tangent vector defined along the interface's border. Unit normal surface vectors, $\boldsymbol{\sigma}$, orthogonal to $\mathbf{u}$, lie on the interfacial surface pointing outward from the domain, so that $(d\Sigma)\mathbf{u}\cdot\boldsymbol{\sigma} = 0$.

Leibniz differentiation of the volume integral in Eq. (7) yields energy rates associated with enthalpy changes and phase transformation in the transport theorem [45,46], namely

$$\frac{d}{dt}\left[\iiint_{\mathcal{D}(t)} H_i(\mathbf{R}_i, t)\, dV_i \right]$$
$$= \iiint_{\mathcal{D}(t)} \left(\frac{\partial H_i(\mathbf{R}_i, t)}{\partial t} \right) dV_i + \iint_{S(t)} (H_\ell - H_c)\mathbf{v}(\mathbf{r}, t)\cdot\mathbf{n}\; dA. \tag{8}$$

The triple volume integral on the right-hand side of Eq. (8) tracks the rate of enthalpy changes within both bulk phases, $i = c, \ell$. The double integral in Eq. (8) accounts for the rate of internal redistribution of transformation enthalpy occurring from any net phase change—i.e., melting or crystal growth—at the interfacial sub-area, $S(t)$, which moves relative to the domain's centroid at its own local normal speed, $\mathbf{v}(\mathbf{r}, t)\cdot\mathbf{n}$.

Again, Leibniz differentiation of the area-weighted energy-rate integral on the left-hand side of Eq. (7) similarly yields several energy exchange rates identified by Gurtin [30] that are associated with moving and deforming interfaces,

$$\frac{d}{dt}\left[\iint_{S(t)} \gamma(\mathbf{n})\, dA \right] = \iint_{S(t)} \left(\frac{\partial \gamma(\mathbf{n})}{\partial t} \right) dA$$
$$+ \iint_{S(t)} \mathcal{H}(\mathbf{r}, t)\gamma(\mathbf{n})\mathbf{v}(\mathbf{r}, t)\cdot\mathbf{n}\; dA. \tag{9}$$

The second integral appearing on the right-hand side of Eq. (9) measures the 'stretching' rate of the expanding or shrinking sub-interface, $S(t)$, by virtue of which $S(t)$ reversibly stores or releases free energy. This term introduces the interface's mean curvature, namely, $\mathcal{H}(\mathbf{r}, t) = \frac{1}{2}\mathrm{Tr}\{\kappa_{ij}\} = \frac{1}{2}(dA/dV)$, as the geometric quantity connecting the rates of area and volume change as the domain's curved sub-interface expands normal to itself and sweeps through $\mathbb{R}^3$ [52].

The technical manipulations of domain contraction and the application of the two-dimensional (surface) divergence theorem to the energy balance are briefly explained in the next section [53,54], the latter providing the standard transformation that converts the line integral in Eq. (7) to an additional area integral of the superficial energy flux over the sub-interface, $S(t)$.

Combining the Leibniz time derivatives on the right-hand sides of Eqs. (8) and (9), and inserting them into the left-hand side of the energy balance, Eq. (7), allows energy conservation to be written in Eq. (10) as sub-volume integrals over V_i within the bulk phases, plus two different area integrals: the first covering the outer boundaries of the domain, $\partial \mathcal{D}(t)$, and the second over the domain's crystal–melt

sub-interface, $S(t)$. These three integrals collectively identify every energy rate process found within or outside the bi-phase domain, $\mathcal{D}(t)$. Conservation of energy thus demands that

$$\iiint_{\mathcal{D}(t)} \frac{\partial H_i(\mathbf{R}_i, t)}{\partial t}dV_i - \iint_{\partial \mathcal{D}(t)} \mathbf{J}_i\cdot\mathbf{N}\; dA + \iint_{S(t)}\left[\frac{\Delta H_f}{\Omega}\mathbf{v}(\mathbf{r})\cdot\mathbf{n} \right.$$
$$\left. + \frac{\partial \gamma(\mathbf{n})}{\partial t} + \mathcal{H}(\mathbf{r}, t)\gamma(\mathbf{n})\mathbf{v}(\mathbf{r})\cdot\mathbf{n} - \nabla_\tau\cdot\mathbf{\Phi}_\tau(\mathbf{r}) \right]dA = 0. \tag{10}$$

Here the ratio $\Delta H_f/\Omega \equiv H_\ell - H_c$ denotes the 'jump' in volumetric enthalpy density upon transformation from the solid to liquid phase, where ΔH_f is the molar enthalpy change (latent heat of fusion), and Ω is the system's molar volume.

As already mentioned, the last term appearing within the integrand of the second area integral in Eq. (10), $-\nabla_\tau\cdot\mathbf{\Phi}_\tau(\mathbf{r})$, represents (minus) the surface divergence of fluxes tangential to the sub-interface—a higher-order energy rate than heat fluxes normal to $\partial D(T)$—which results from application of the surface divergence theorem to the line integral in Eq. (7) of any superficial flux component exiting, or entering, the domain anywhere round its border . This energy rate appears in the Reynolds balance because it represents the net energy loss or gain from $S(t)$ along the closed border of its sub-interface, $\partial S(t)$. The surface divergence operator, $\nabla_\tau[\cdots]$, is a *dimensional* vector operator that acts parallel to the *dimensionless* unit tangent vector, $\boldsymbol{\tau}$, along that border. Again, as discussed earlier in Section 3.2, the tangential flux itself unavoidably arises on crystal–melt interfaces as a direct response to gradients impressed by the GTH potential distribution along those interfaces. The surface 'convergence' of that tangential flux, $-\nabla_\tau\cdot\mathbf{\Phi}_\tau(\mathbf{r})$, is a scalar energy rate that we have termed the capillary-mediated 'bias field'—a short descriptive name chosen as suggestive of its thermodynamic function to bias, or otherwise perturb, the local rates of melting or crystallization by addition or removal of capillary-driven energy.

We now show how the bias field enters the energy balance for the interface and stimulates shape changes[4] during either melting or crystal growth under local equilibrium.

4.4. Domain contraction

Energy conservation, as developed specifically here for the bi-phase domain considered in Section 4.3, can be further constrained to include only those rates related to motion of the sub-interface itself. This constraint may be imposed rigorously through the process of 'contraction mapping' the bi-phase domain along its exterior normals, $\mathbf{N}$, over the its entire *outer* boundary $\partial \mathcal{D}(t)$. Contraction mapping withdraws $\partial \mathcal{D}(t)$ closer and closer toward the *internal* sub-interface, $S(t)$, separating the solid and liquid bulk phases. Domain contraction taken to its limit conveniently allows all energy contributions from the phase sub-volumes to vanish, because $V_i \to 0$, which eliminates energy rates contributed from the volume-weighted integrals, but retains all contributions from the area-weighted integrals.

Domain contraction is accomplished mathematically when the outer domain boundary conforms to the contraction mapping, $\mathfrak{C}: \partial D(t)\mapsto S(t)$. Thus, full domain contraction also equates the

---

[4] The 2-D interfaces selected subsequently for further analysis in this study are analytic planar curves (vector-valued functions of one variable, e.g., conic sections [52]). In $\mathbb{R}^3$, therefore, they form manifolds with zero Gaussian curvature, $\mathcal{K}$ (i.e., ruled surfaces), where $\mathcal{K} = \mathrm{Det}\{\kappa_{ij}\} = 0$ [36]. Interfaces described by plane curves in $\mathbb{R}^2$, have capillary-mediated fluxes that vary with just one normal angle, φ, and result in a single, in-plane curvature, $\kappa(\varphi)$. See again Section 3.3 and (1) for interface shapes that evolve in $\mathbb{R}^2$. Interfaces in 3-D, which are modeled as curved surface patches, exhibit two principal curvatures that combine as the mean curvature, $\mathcal{H}(\mathbf{r})$. The mean curvature itself generally depends on two normal angles defined along an interface's orthogonal surface coordinates [36].

limits of the two area integrals appearing in Eq. (10), allowing (1) elimination of the volumetric integral, and (2) combination of the integrands, $J_i \cdot \mathbf{N}$ ($i = c, \ell$), from the first area integral with the integrand from the second sub-interface integral. Domain contraction, in addition, forces the exterior unit normals on $\partial \mathcal{D}(t)$ to re-configure their orientations and align with those covering the sub-interface, $\mathcal{S}(t)$, according to the vector mapping, $\mathfrak{N}: \mathbf{N} \mapsto \mathbf{n}$.

One is left after domain contraction with an infinitesimally thin control space, embedded in $\mathbb{R}^3$, and conforming precisely to the sub-interface $\mathcal{S}(t)$. The contracted control space in 3-D, (1) monitors all superficial flux components, both tangential and normal to $\mathcal{S}(t)$; (2) accounts for any energy storage or release associated with interfacial stretching or contraction of the sub-interface; and (3) tracks the production or absorption of latent heat from normal interface motion, i.e., phase change. Most importantly, however, application of domain contraction provides a single, area-weighted integral that conserves all energy rates associated with changes in an interface's area and orientation experienced during quasi-static phase transformation.

Domain contraction provides the Leibniz–Reynolds *interfacial* energy balance for an arbitrary interface evolving at local equilibrium. The resultant balance is an area-weighted integral of every relevant energy rate, namely

$$\iint_{\mathcal{S}(t)} \left[-\sum_{i=s}^{\ell} \mathbf{J}_i \cdot \mathbf{n} + \frac{\Delta H_f}{\Omega} \mathbf{v}(\mathbf{r}) \cdot \mathbf{n} + \frac{\partial \gamma(\mathbf{n})}{\partial t} \right.$$
$$\left. + \mathcal{H}(\mathbf{r}, t) \gamma(\mathbf{n}) \mathbf{v}(\mathbf{r}) \cdot \mathbf{n} - \nabla_\tau \cdot \mathbf{\Phi}_\tau(\mathbf{r}) \right] \times dA = 0. \tag{11}$$

Conservation of energy requires that the integrand in Eq. (11) vanishes over the sub-interface, $\mathcal{S}(t)$. Given that the limits of integration are arbitrary, the following energy rates, re-grouped slightly from those appearing in Eq. (11), must collectively cancel at *all* continuum area scales on interfaces in either 3-D or 2-D:

$$\frac{\partial \gamma(\mathbf{n})}{\partial t} + \left(\frac{\Delta H_f}{\Omega} \mathbf{v}(\mathbf{r}) + \mathcal{H}(\mathbf{r}, t) \gamma(\mathbf{n}) \mathbf{v}(\mathbf{r}) \right.$$
$$\left. - \mathbf{J}_c - \mathbf{J}_\ell \right) \cdot \mathbf{n} - \nabla_\tau \cdot \mathbf{\Phi}_\tau(\mathbf{r}) = 0. \tag{12}$$

Consistent with Eq. (12), a dynamic solid–liquid interface will generally involve the following energy rates:

1. Time rate of interfacial energy density change with crystallographic orientation, $\mathbf{n}$;
2. Latent heat absorption or production from phase change, and energy storage or release from stretching/shrinking the interface—both of which rates are proportional to the normal interface speed, $\mathbf{v}(\mathbf{r}) \cdot \mathbf{n}$;
3. Heat flow, $\mathbf{J}_i \cdot \mathbf{n}$, ($i = c, \ell$) into the surrounding solid and liquid phases along local gradients parallel to $\mathbf{n}$;
4. Capillary-mediated energy, added or removed, which is equal to minus the surface divergence of the tangential flux, $\mathbf{\Phi}_\tau(\mathbf{r})$, driven by gradients in the GTH interface potential.

Excepting rate (4), the other energy rates are associated with either *normal directions*, $\mathbf{n}$, or *normal* motions, $\mathbf{v}(\mathbf{r}) \cdot \mathbf{n}$, of the interface. Rate (4) is uniquely related to the existence of capillary-mediated *tangential* heat fluxes that are stimulated as a result of local equilibrium conditions associated with the varying interface potential.

4.5. Interfacial equilibrium and size-scale

Two further physical constraints may be imposed on the general Leibniz–Reynolds conservation condition developed in Eq.

(12). These constraints help reveal more clearly the interplay between macroscopic gradients, microscopic energy sources, and superficial and normal fluxes, all of which interact and influence the dynamics of evolving interfaces:

1. The interface, as a consequence of local equilibrium, requires that every sub-interface, or surface patch comprising the interface stores free energy. The local area density of that energy, $\gamma(\mathbf{n})$, depends *uniquely* on the patch's instantaneous spatial orientation relative to the underlying crystal axes. Specifically, as interface patches evolve, their local orientation may indeed change over time. Their free energy densities, however, are a function solely of their instantaneous crystallographic orientation and, therefore, $\gamma(\mathbf{n})$ is not an explicit function of time[5]; so, its partial derivative with respect to time vanishes at a constant orientation, $\mathbf{n}$. This consequence of local interfacial equilibrium eliminates from further consideration the time derivative in Eq. (12), listed as energy rate (1) compiled at the end of Section 4.4.
2. The interfacial 'stretching' rate, which was also listed as part of energy rate (2) in the enumeration listed above, is the term, $\mathcal{H}(\mathbf{r}, t) \gamma(\mathbf{n}) \mathbf{v}(\mathbf{r}) \cdot \mathbf{n}$, appearing in Eq. (12). Its value is generally non-zero, but it too may be otherwise safely discounted, unless the product of local curvature and energy density, $\mathcal{H}(\mathbf{r}, t) \gamma(\mathbf{n})$, were to become large enough to be comparable to the volumetric latent heat, $\Delta H_f/\Omega$. A proportionate comparison between latent heat generation and interface 'stretching' rates is fully justified, inasmuch as both these rates are proportional to the normal velocity times the energy per unit volume (either as latent heat per unit volume transformed, or as energy per unit area change of the interface). The mean curvature, therefore, would have to achieve a magnitude approaching that of the reciprocal capillary length, estimated as $1/\lambda_{cap} \approx 10^9 \text{ m}^{-1}$ for most systems, so that interfacial stretching might sensibly modify the rate of latent heat release. Again, this remains valid as latent heat and interface stretching rates are *both* proportional to the interface's normal speed. In the case of crystal–melt systems that involve either small melting crystallites, or growing crystals exhibiting mesoscopic structures such as cells, dendrites, and eutectics, the largest local curvatures encountered seldom ever exceed 10^7 m^{-1}. Thus, one concludes, interface 'stretching' during either melting or crystal growth may be considered as a relatively inconsequential (proportionate) correction to latent heat absorption or production, having an insignificant effect on the net amount of phase change. Moreover, although its inclusion does imperceptibly affect the total amount of phase transformation, interfacial stretching energies by themselves do not seem to influence interfacial patterns at mesoscopic scales.

4.6. Interface energy balances

4.6.1. Leibniz–Reynolds energy balance

One concludes on the basis of these additional physical assumptions that during solid–liquid transformation under local equilibrium interface energy conservation requires a balance among three distinct energy rates: (1) latent heat released, or absorbed; (2) heat conducted to or from the adjacent phases; (3) energy deposited or removed by divergent or convergent interfacial fluxes.

The interface energy balance that remains valid at *all* continuum length scales, according to the foregoing Leibniz–Reynolds

---

[5] The identical argument based on local interface equilibrium and orientation is employed by W.W. Mullins in his theory of surface thermal grooving kinetics [48].

analysis, is given as

$$\left(-\mathbf{J}_c - \mathbf{J}_\ell + \frac{\Delta H_f}{\Omega}\mathbf{v}(\mathbf{r})\right)\cdot\mathbf{n} - \nabla_\tau\cdot\mathbf{\Phi}_\tau(\mathbf{r}) = 0. \tag{13}$$

The terms within large parentheses in Eq. (13) exclude capillarity, and are capable of balancing one another over large (macroscopic) length scales. These terms, in fact, do determine the overall rate of solid–liquid phase change. Note that all of these energy rates couple to the *normal* direction or *normal* motion of the interface. However, the conduction fluxes involve macroscopic gradients, whereas the latent heat involves transition energies arising from microscopic processes occurring at the interface. The last term in Eq. (13), which is the bias field, arises from capillary-mediated *tangential* interface fluxes that have no obvious influence on the energy balance occurring normal to the interface at longer length scales.

Dynamic arguments indicate, however, that over smaller time intervals and mesoscopic length scales the tangential bias-field term couples to and slightly modifies the latent heat rate. In fact, it is the *algebraic sum* of these two microscopic source terms that actually must balance with the slower changing transport fluxes, especially at mesoscopic length scales where patterns development occur. Also, for reasons to be explained later, the tangential term elicits little or no influence on the energy balance occurring over larger macroscopic scales! The energy rates derived from the divergence or convergence of the tangential flux are deterministically self-induced by virtue of the interface's instantaneous shape and orientation. As shown next these self-generated (autogenous) energy rates are essential to pattern initiation during unstable crystal growth, and to modifying the dynamic shapes of melting crystallites.

The bulk phase conduction fluxes, $\mathbf{J}_i$ ($i = c, \ell$), appearing in Eq. (13) may be evaluated by applying Fourier's law again [40], where

$$\mathbf{J}_i = -k_i\nabla[T_i]_{S(t)}, \quad (i = c, \ell). \tag{14}$$

The line integral which follows on the right-hand side of Eq. (7) tracks energy leaving or entering through the border, $\partial S(t)$, of the solid-liquid sub-interface, $S(t)$. The transport coefficients, k_i, connecting conduction fluxes and gradients are the usual thermal conductivities of the adjacent bulk phases. If the gradient vector within the adjacent solid or liquid phase points toward the interface, its sign is conventionally taken as positive—a convention consistent with crystal growth occurring when net heat is conducted *away* from the interface, and melting when net heat is conducted *toward* the interface.[6]

Expanding Eq. (14), and inserting that result into Eq. (13), yields the Leibniz–Reynolds 'omnimetric' interface energy rate balance, which is the exact energy balance applicable to *continuum* length scales:

$$k_c\nabla[T_c]_{S(t)}\cdot\mathbf{n} + k_\ell\nabla[T_\ell]_{S(t)}\cdot\mathbf{n} + \frac{\Delta H_f}{\Omega}\mathbf{v}(\mathbf{r})\cdot\mathbf{n} - \nabla_\tau\cdot\mathbf{\Phi}_\tau(\mathbf{r}) = 0. \tag{15}$$

The first three terms in Eq. (15) provide the standard Stefan energy balance that appears in conventional descriptions of freezing and crystal growth [41,42], where the net rates of heat conduction into the surrounding bulk phases balance latent heat production. An important point to be noted here is that eliminating the tangential flux divergence rate in Eq. (15) to recover the conventional Stefan balance is tantamount *at short time scales* to assuming that the

interfacial energy density $\gamma_0 = 0$, so the capillary flux and its divergence both vanish. As will be shown, when averaged over long length scales the capillary flux divergence vanishes. These special features provide likely reasons that capillary-mediated energies have not been included in interfacial energy balances. Capillarity, when it is included in phase-change problems, is often relegated to a boundary condition connecting curvature, temperature, and concentration, rather than recognizing the capillary-mediated flux divergence as a physically *active* energy source. The critically important distinction established here between interface energy balances at mesoscopic and macroscopic length scales—heretofore overlooked—will now be clarified by considering interface dynamics.

4.6.2. Standard energy balance

The conventional Stefan balance, although valid at macroscopic scales, lacks the capillary-mediated energy term required for exact energy conservation at shorter length scales. Stefan balances for either energy or species simply overlook the short-range perturbation field that exists at mesoscopic scales, and which accounts for pattern initiation. Conventional Stefan balances provide information only relevant to the net amount of phase transformation, not the autogenous perturbations.

$$k_c\nabla[T_c]_{S(t)}\cdot\mathbf{n} + k_\ell\nabla[T_\ell]_{S(t)}\cdot\mathbf{n} = -\frac{\Delta H_f}{\Omega}\mathbf{v}_0(\mathbf{r})\cdot\mathbf{n}. \tag{16}$$

A subscript "0" is appended to the interface velocity, $\mathbf{v}_0(\mathbf{r})$, that multiplies the volumetric latent heat to give the latent heat rate in the Stefan balance, Eq. (16). That subscript denotes that effects arising from capillarity are removed in formulating the interface speed, $\mathbf{v}_0(\mathbf{r})\cdot\mathbf{n}$, which is valid at large length scales. Again, we emphasize that Eq. (16) accounts correctly for the *overall* rate of phase change. Moreover, this balance gives a result that comports fully with conventional arguments reviewed in Section 3.3, where energy rates were included only from terms that couple through the interface's normal vector, $\mathbf{n}$. We now add back the one energy rate that does not couple through the normal transport field, namely the capillary bias field.

4.6.3. Omnimetric energy balance

A term identified in the Leibniz–Reynolds energy rate balance, Eq. (15), but excluded from the Stefan balance, Eq. (16), accounts for the 4th-order capillarity-dependent energy rate associated with the interface's tangential flux. This term actually perturbs the speed of an interface over relatively short time and length scales by inducing small compensatory adjustments to the local rate of latent heat production. Substituting the right-hand side of Eq. (16) for the two conduction terms in the full omnimetric Leibniz–Reynolds balance, Eq. (15), defines the scalar bias-field function, $B(\mathbf{r})$, as the superficial divergence of the vector tangential flux, and relates it to local interface dynamics mediated by capillarity.

The omnimetric energy rate balance, valid over *all* continuum length scales, shows the following important dynamic relationship

$$B(\mathbf{r}) \equiv -\nabla_\tau\cdot[\mathbf{\Phi}_\tau(\eta, \xi)] = \frac{\Delta H_f}{\Omega}\left[\mathbf{v}_0(\mathbf{r}) - \mathbf{v}(\mathbf{r})\right]\cdot\mathbf{n}. \tag{17}$$

Eq. (17) specifies that small velocity shifts, $\mathbf{v}_0(\mathbf{r}) - \mathbf{v}(\mathbf{r})$, are expected that are 4th-order perturbations, once capillary-mediated energies are included in the omnimetric interfacial energy rate balance. Moreover, as indicated, the bias field energy rate is itself proportional to, and of the same order, as the speed perturbations it causes.

Thus, inclusion of the bias field energy rate allows capillary-mediated energy losses and gains to occur on short time scales to produce autogenous speed perturbations, which on unstable

---

[6] More precisely, crystal growth requires the conductivity-weighted gradients surrounding the interface be positive, so the normal interface speed, $\mathbf{v}(\mathbf{r})\cdot\mathbf{n} > 0$, whereas melting requires that the conductivity-weighted gradients be negative, and $\mathbf{v}(\mathbf{r})\cdot\mathbf{n} < 0$. Also, for unconstrained (unstable) crystal growth, or (stable) melting, it is the thermal field in the surrounding melt that regulates those rates, whereas for directional crystallization of a pure material it is the thermal field in the solid that dominates heat transfer from the moving interface [55].

interfaces will be shown to initiate interface modulations in the form of branching and enhanced pattern complexity. These dynamical aspects of the bias field will now be addressed in further detail.

5. Capillary bias fields

5.1. The scalar field

We now return to the initial task of finding a general expression in 2-D for the bias field, $B(\varphi)$, parameterized with the normal angle coordinate along an in-plane interface in $\mathbb{R}^2$. From Eq. (17) that defines the bias field operationally, one substitutes its equivalent divergence operations in $\mathbb{R}^2$, namely

$$B(\varphi) \equiv -\nabla_\tau \cdot [\Phi_\tau(\varphi)] = \beta \frac{d}{d\varphi}\left[\frac{d}{d\varphi}[\vartheta(\varphi)] \times \hat{k}(\varphi)\right] \times \hat{k}(\varphi), \tag{18}$$

where the bias field constant, β, located on the right-hand side of Eq. (18) is the dimensional coefficient defined as $\beta \equiv \frac{K_{int}\gamma_0\Omega}{a^3\Delta S_f}$ [W/m^2]. This materials/system constant re-introduces the dimensionless curvature, $\hat{k}(\varphi) = a\kappa(\varphi)$, and also non-dimensionalizes the arc-length divergence operator, $\nabla_\tau[\cdots]$, by inserting a^3 into the denominator of β. One finds that minus the arc-length divergence defined in Eq. (18) is the 'convergence' in 2-D of the tangential GTH flux. As shown on the right hand side of Eq. (18), the flux convergence is found by differentiating the expression for the capillary-mediated tangential flux with respect to the normal angle, as already derived in Eq. (6). Application of the chain rule once more by multiplying that angular derivative by the in-plane curvature, $\kappa(\varphi) = \frac{d\varphi}{ds}$, provides the desired result.

The above mathematical steps yield a general expression for the dimensional bias field, $B(\varphi)$, on an arbitrary 2-D solid–liquid interface supporting energy density anisotropy, viz.

$$B(\varphi) = -\left(\frac{K_{int}\gamma_0\Omega}{\Delta S_f}\right)\kappa^3(\varphi)\Gamma(\varphi). \tag{19}$$

The auxiliary function, $\Gamma(\varphi)$, introduced in Eq. (19), contains the nonlinear interplay between shape (curvature variations) and energy density anisotropy, both of which play roles in the dynamic evolution of interfaces. The function $\Gamma(\varphi)$ is defined as the following 4th-order expression relating the interface shape, energy density, and the bias field, $B(\varphi)$,

$$\Gamma(\varphi) \equiv \left(\frac{\gamma_{\varphi,\varphi} + \gamma_{\varphi,\varphi,\varphi,\varphi}}{\gamma_0}\right) + 3\left(\frac{\gamma_\varphi + \gamma_{\varphi,\varphi,\varphi}}{\gamma_0}\right)\frac{\kappa_\varphi}{\kappa(\varphi)}$$
$$+ \frac{\gamma(\varphi) + \gamma_{\varphi,\varphi}}{\gamma_0}\left(\frac{\kappa_{\varphi\varphi}}{\kappa(\varphi)} + \frac{\kappa_\varphi^2}{\kappa^2(\varphi)}\right). \tag{20}$$

A dimensionless form of the bias field, $\mathfrak{B}(\varphi) \equiv B(\varphi)/\beta$, convenient for analysis and comparison with numerical models, results from dividing both sides of Eq. (18) by β. Thus, in 2-D, this intrinsic thermodynamic scalar field may be expressed as

$$\mathfrak{B}(\varphi) = -\hat{k}^3(\varphi)\Gamma(\varphi). \tag{21}$$

One notes that the strength of bias field perturbations increases rapidly as interface curvature cubed, (i.e., inversely as feature size cubed, a^{-3}). Bias-field perturbations appear during melting or growth as a result of either the interface shape or the energy anisotropy acting alone, or simultaneously.

Analytic use of Eq. (21) requires that the interface shape, $c(x, y) = c(s(\varphi)) = 0$, and its energy anisotropy, $\gamma(\varphi)$, each be 4th-order differentiable, whereas numerical models capable of

resolving bias field perturbations on general evolving interfaces should be 4th-order accurate. These requirements suggest that the bias field is analogous to surface species diffusion, by which W.W. Mullins analyzed the kinetics of thermal grooving on a crystal–vapor surface almost 60 years ago using related principles [48].

5.2. Field theoretic properties

5.2.1. Interface Poisson equation and associated fields

The bias field represents the instantaneous energy rate deposited or removed from a dynamic interface in concert with local equilibrium. The tangential flux responsible for the bias field is a 'conservative', i.e., path-independent vector field. That flux is proportionate and anti-parallel to the gradient of the scalar potential supporting that field, so $\Phi_\tau[\vartheta(\varphi, t)]$.

The set of theoretical linkages from field theory that connect the GTH scalar thermo-potential, $\vartheta(\varphi, t)$, to its tangential vector flux, $\Phi_\tau(\varphi, t)$, and from tangential flux to its scalar convergence, or bias field, $\mathfrak{B}(\varphi)$, shows that a superficial Poisson equation exists, which connects the interface's scalar GTH thermo-potential to its associated bias field. The superficial Poisson equation in 2-D that links these interrelated scalar interface fields is

$$\mathfrak{B}(\varphi) = \nabla_\tau^2\left[\vartheta(\varphi)\right]. \tag{22}$$

Line integrals of the vector tangential flux vanish over a closed curve in 2-D that follows the evolving interface. This mathematical property is also responsible for making detection of bias field energies in 3-D impossible by bulk calorimetry, as the line integral of its associated vector field taken round the interface supporting its scalar potential exactly vanishes in $\mathbb{R}^n$ [56].

One finds that capillary-mediated tangential flux obeys the 'path-independent' property for conservative fields, namely that the closed line integral of this vector field taken round a closed interface vanishes, so that

$$\oint_c (\Phi_\tau(\varphi)\cdot\tau)\, ds = 0. \tag{23}$$

The scalar bias field, as proven next, also shares this property of global neutrality and, therefore, does not alter the average amount of phase transformation as time progresses. The bias field acts instead as an autogenous energy source that perturbs the local interface speed and modulates the interface's shape on smaller length scales, where its value is locally non-zero and varies in strength and sign. The author further suggests that this scale-dependent property provides the fundamental reason why neither experiments, nor numerical models, detect a noticeable difference between the Stefan balance that ignores capillarity, namely, Eq. (16), and the omnimetric energy balance derived here in Section 4.6 using the Leibniz–Reynolds theorem. It also appears that precise IDGE microgravity experiments flown by NASA were the first to support experimental conditions allowing, by direct observation and measurement, detection of shape-altering effects on melting crystallites from an intrinsic capillary-mediated interfacial energy field.

5.2.2. Macroscopic effects of the bias field

In 2-D, the dimensionless bias field, $\mathfrak{B}(\varphi)$, may be expressed in several mathematical forms by employing normal-angle and arclength parameterizations for the flux, for which $\Phi(\varphi)$ represents the magnitude of the vector tangential flux, $\Phi_\tau(\varphi)$, at an arbitrary interfacial location with normal angle φ. The dimensionless bias field in 2-D, defined from Eqs. (18) and (21) as the convergence of the tangential vector flux, may be equated to the nested product of derivatives and curvatures—all functions of φ.

$$\mathfrak{B}(\varphi) \equiv - \nabla_\tau \cdot [\Phi(\varphi)\boldsymbol{\tau}] = - \frac{d}{d\varphi}\left[\frac{d}{d\varphi}[\vartheta(\varphi)] \times \hat{k}(\varphi) \right] \times \hat{k}(\varphi). \tag{24}$$

That the total amount of capillary energy released over the entire arc length of the interface averages to zero can now be proved following these steps: (1) reverse the order of differentiation and integration, which is interchangeable for uniformly continuous functions on bounded closed domains, then (2) apply Eq. (23), which shows that a closed line integral of the path-independent tangential flux vanishes. Thus, one finds

$$\oint_c \nabla_s \cdot \boldsymbol{\Phi}_\tau(\varphi) \, ds = \oint_c \frac{d}{d\varphi}\left[\{\Phi(\varphi)\boldsymbol{\tau}\} \cdot \boldsymbol{\tau} \right] ds \times \kappa(\varphi)$$
$$= \frac{d}{d\varphi}\left[\oint_c \boldsymbol{\Phi}_\tau(\varphi) \cdot \boldsymbol{\tau} \, ds = 0 \right] \kappa(\varphi) = 0. \tag{25}$$

Equalities (25) suggest why bias-field energy has gone unnoticed: it lacks influence on the total (macroscopic) amount of phase transformation as time increases. Yet, the bias field, as to be shown next, plays a decisive role in providing pattern-forming *mesoscopic* perturbations on the interface speed, which, as just explained, average to zero on long scales.

As was postulated 35 years ago [57], and broadly accepted for over two decades [58], the creation of many diffusion-limited crystallization microstructures, such as the mesoscopic patterns typifying alloy dendrites, mineral forms, frost and snowflakes, are all attributed to 'selectively amplified noise'. Choosing stochastic processes as being primarily causal for diffusion-limited pattern formation was indeed understandable, as deterministic perturbations arise from 4th-order thermodynamic energies, the very presence of which is obscured because their system-wide macroscopic average is zero. Intrinsic perturbations, as will be demonstrated, act through autogenous means, influence interface conditions, and predispose the evolution of complex interfacial patterns. Bias field energy, moreover, provides fully deterministic intrinsic perturbations that when combined with interfacial stability act independently from extrinsic stochastic disturbances, induced by crystallographic defects, environmental stimuli, or noise.

5.3. Time and length scales

Capillary bias fields depend on subtle geometric and thermodynamic characteristics of the solid–liquid interface, over which they redistribute small amounts of thermal energy. These energy sources and sinks cause speed perturbations, because capillary energy exerts a prompt influence on local dynamics, inducing at mesoscopic scales both evolutionary modulations that lead to enhanced complexity of the interface. We now examine how such a subtle energy field controls dynamic modulation on active interfaces.

First, one notes that the source terms found in the interface Leibniz–Reynolds energy balance, Eq. (15), which derive from independent, but ultimately, *coupled* microscopic interface phenomena include: (1) latent heat production/absorption, and (2) local equilibrium redistribution of capillary energy via the bias field. Next, the time scales associated with each of these interface energy sources are extremely brief. Short response times arise because latent heat is released at an interface as molecules depart the liquid phase to join the crystal, or, vice versa, latent heat is instantly absorbed where melting prevails and molecules leave the crystal. Either process, melting or freezing, involves short-range unimolecular events. Similarly, so do bias field energy redistributions, as they arise to satisfy local equilibrium by adjusting the chemical potentials of the molecules proximate to the interface. Given that local equilibrium involves relatively few molecules adjoining a moving interface, their time scale for exchanging energy also remains extremely brief. Indeed, both experiments and

modeling confirm that mobile (kinetically unhindered) solid–liquid interfaces compensate departures from local equilibrium in time intervals no longer than about 1–10 μs [59,60].

Contrasting the microscopic nature of interface energy sources, energy transport (e.g., heat conduction) to and from the interface depends on long-range *macroscopic* gradients. Gradients included in the interface energy balance adjust relatively slowly[7] within the bulk phases adjoining the interface. The reason for this slow response is that conduction gradients involve interactions that extend far from the interface. Transport gradients, consequently, tend to evolve on much longer time scales during phase transformation relative to those associated with interfacial energy sources. In fact, the macro-gradient fields assisting transport through the bulk phases usually change so slowly relative to change rates for microscopic energy sources that the former act as nearly stationary, or quasi-static, thermal features during those brief periods required by adjustments for the microscopic interface processes. The large disparity in these coupled time scales for fast changing energy sources and slow changing transport gradients accounts for the dynamic behavior of intrinsic perturbations arising from relatively weak bias fields. In accord with the principle of energy conservation, macroscopic transport gradients remain in balance with the *sum* of two independent energy rates from interface sources. This balance must be maintained during either melting or growth between heat transported through macro-gradients adjacent to the interface and the momentary sum of the (strong) latent heat source plus the (weak) capillary bias field. This dynamic energy rate balance, moreover, must hold even over periods where brief adjustments arise along an evolving interface caused by changes in its shape and thermodynamic potential. Despite the disparity in their respective characteristic time scales between nearly 'fixed' macroscopic and fast-changing microscopic energy rates, a local balance nonetheless must *always* prevail. The microscopic energy sources each arise from independent effects: latent heat rates that are strictly proportional to the interface's normal speed, and capillary bias energy rates that depend non-linearly on the interface's local shape and crystallographic orientation. Energy conservation requires that their sum balance with the conduction rates set over longer time scales by slowly changing macro-gradients surrounding the interface.

The outgoing total heat production rate from the interface during crystal growth into the fixed conduction fields in the adjacent bulk phases remains steady over short time scales. Were the bias field to became more positive from some shift in local equilibrium, and thereby increase the total energy rate released from the interface, then conservation of energy to the quasi-static conduction fields would be compromised. Instead, the interface's speed de-accelerates, promptly reducing latent heat production and thereby satisfying the local interfacial energy balance. Should the bias field be reduced in response to local equilibrium, and lower the total energy release rate from the interface, balance with the adjacent transport fields is immediately restored by boosting the local growth speed to increase the latent heat rate. This action/counter-action compensates dynamically for the bias field's independently driven energy rate changes, and maintains local energy conservation over short adjustment periods along the interface. The capillary bias

---

[7] The characteristic time scale for thermal conduction through a bulk phase via macro-gradients is roughly the ratio of the square of thermal boundary layer thickness, to the thermal diffusivity, Λ^2/D_{th}. Even for an excellent thermally conducting solid phase, with $D_{th} \approx 100 \text{ mm}^2 \text{ s}^{-1}$, which is growing with a thin boundary layer of $\Lambda \approx 0.1 \text{ mm}$, the characteristic thermal adjustment time is roughly 1 ms. That adjustment still takes 100–1000 times longer than the characteristic interaction times for the two source terms, latent heat and bias-field energy.

field induces compensatory perturbations in this coupled inter-active manner on the interface speed that adjusts the local latent heat rate to restore energy balance. The auto-induced local speed perturbations appear as modulations of the interface shape that can subsequently amplify and stimulate the development of complex patterns on unstable interfaces.

Comparable compensation occurs during melting between latent heat absorption rates and variations in the bias field responding to shifts in local equilibrium. These interface perturbations lead precisely to crystallite shape modifications as were observed during conduction-limited melting in microgravity.

5.4. Laplace points

The capillary bias field, $\mathfrak{B}(\varphi)$, can vanish in 2-D on interfaces at isolated interfacial orientations, $\varphi^\star$, where the governing surface Poisson relation, Eq. (22), reverts locally to the surface Laplace equation, where $\nabla^2_\tau[\vartheta(\varphi)] = 0$. The sign of the bias-field energy rate reverses at these isolated zero points, which are the roots of the scalar flux divergence. These roots have dramatic influences on the interface dynamics, as they can lead to inflection, branching, and other pattern variations. They are designated as bias field 'Laplace points'.

Laplace points are particularly interesting features of the bias field, insofar as equilibrium is satisfied locally at those points, without any subsequent changes needed in the local interfacial curvature. This situation occurs where the bias field $\mathfrak{B}(\varphi^\star) = -\kappa(\varphi^\star)\Gamma(\varphi^\star) = 0$, and $\kappa(\varphi^\star) \neq 0$. Surrounding each such Laplace point in 2-D there exists a small neighborhood, or angular region, $\pm\delta\varphi$, subject to increasing—but opposing—speed perturbations, $\pm\delta v_n(\mathbf{r})$. Opposing speed perturbations on each side of a Laplace point reverse the time rates of change for the adjacent interface curvatures. If amplified by the external transport field, countervailing curvature changes on the interface eventually develops a rotation, or 'curl', surrounding the Laplace point where $\kappa \to 0$.

Adjacency information along a continuous interface is spread by second derivatives of the normal speed that depend[8] on $\frac{d^2B}{ds^2}$, which slow and flatten the interface where $\mathfrak{B}(\varphi) > 0$, and nearby each Laplace point, where $\mathfrak{B}(\varphi) < 0$, accelerate and sharpen the interface. These autonomous curvature responses have a classical, if somewhat unusual, thermodynamic interpretation.

Inasmuch as the bias field energy depends on the interface curvature, the coupled responses between the chemical potential and changes in interface curvature represent an unusual form of the Le Chatelier–Braun effect [25,26], where internal system variables subject to a local change—in this instance a purely geometric variable of the interface—spontaneously respond in a direction that always tends to restore the system locally toward equilibrium. Le Chatelier–Braun responses over a small region surrounding bias-field Laplace points cause simultaneous curvature flattening and sharpening that eventually inflect the interface. If such an inflection develops on an unstable interface, it can amplify to form a bump, or cause invagination, folding, and even splitting—all of which contribute to increased pattern complexity. Some examples of various inflective perturbations induced by bias field perturbations at Laplace points are presented in the next section.

---

8 Our overall description of pattern formation suggests that the thermo-dynamic fields responsible for pattern development depend up to the 4th derivative of the interface curvature, which involve derivatives of the interface shape up to 6th-order! These high-order dependencies on the pattern form doubtless interfere with the detection of the bias field through ordinary experimental and numerical methods.

6. Analytical and numerical models

6.1. Background

In 2006, capillary phenomena were initially suspected as responsible for shape modifications observed during melting in microgravity. The author desired an analysis of the behavior of Gibbs–Thomson–Herring potentials on anisotropic ellipsoidal crystal–melt interfaces. High-aspect ellipsoids closely approximated the shapes of melting crystallites in microgravity observed in the IDGE experiments. That mathematical analysis was performed by McFadden [61], who used methods based on variational calculus to confirm independently the development of non-monotone thermo-potentials on anisotropic crystalline ellipsoids melting in microgravity. McFadden's analytical results for the thermo-potential in 3-D, combined with precision microgravity melting data discussed in Section 1, supported the author's hypothesis that autogenous capillary fields might be capable of perturbing solid–liquid interfaces and be linked to pattern formation.

Bias fields on 2-D interfaces have now been explored extensively by the author applying the mathematical results outlined in this paper to a variety of analytic shapes. These studies exposed and confirmed the general properties derived for the bias field, such as the presence of Laplace points close to the tips of finger-like protuberances; countervailing dynamic curvature changes surrounding each Laplace points; neutrality of the bias field at macroscopic scales; and, most importantly, the stimulation of pattern complexity from smooth starting shapes.

As the bias field is just a higher-order spontaneous result of the chemical potential, standard numerical models of interface dynamics, e.g., phase field, level sets, and front tracking, in principle, should already include it within their physics. This is not surprising, given that competent numerical models are thermodynamically consistent in conserving energy and mass and tracking entropy production. However, one encounters certain realities of numerical models when simulating crystal growth, including limited numerical precision caused by truncation and round-off; restricted precision of the computational stencils introduced by discrete approximations for derivatives and curvatures; plus other technical difficulties associated with grid resolution; false anisotropy; and inclusion of inadvertent and even purposely added random noise [62,63]. Such numerical issues apparently conspired to mask, or overshadow, the fundamental cause of pattern evolution by perturbations intrinsically provided by thermodynamics.

Exact predictions derived for bias-fields on various 2-D conic sections and on some transcendental interface shapes, as well as data obtained from melting experiments, were first checked against independent results obtained from several numerical models. More recently we added detailed quantitative checks between predictions from analytical bias-field theory and quantitative simulation data obtained using a dynamical numeric model [64]. Once it was understood that the interface perturbations from capillary fields do indeed entail 4th-order capillary-mediated energy distributions, additional numerical results were provided by independent collaborators that are specifically tailored for the detection of autogenous modulations, including observation of how added random noise influences such patterns.

6.2. Exploring the bias field numerically

Bias field energy distributions derived here analytically from basic thermodynamic principles are already incorporated into the physics of phase-field formulations, as well as with other thermodynamically-consistent numerical models involving sharp interfaces. These capillary fields operate in the background and do not require any additional information or adjustments when simulating pattern evolution.

6.2.1. Interface modulations and fluxes

The first examples of 4th-order accurate, noise-suppressed phase-field simulations are credited to Mullis [65,66], an example of which is shown in Fig. 3. Mullis's numerical simulations supplied the first 2-D phase-field renderings that were sufficiently accurate to reveal the emergence of 4-fold symmetric autogenous perturbations. Mullis also determined the interface temperature field and measured its tangential heat flux along an advancing dendrite tip. The simulated dendrite tip exhibited a faintly pulsating shape, resembling that of the starting parabolic 'finger', with a slightly smaller steady-state tip radius and trailing modulations.

Fig. 4 provides a comparison between Mullis's published interfacial flux measurements with the tangential flux, $\Phi(x/\rho_{para})$, calculated analytically by the author from Eq. (6) for a parabola with the same 4-fold energy density anisotropy. The analytic parabola, $y^2 = -4ax$ ($-\infty < x \le 0$), has a tip radius $\rho_{para} = a/2$, with 4-fold energy density anisotropy chosen identical in strength (3%) to that of the simulated dendrite [66]. This simulated dendrite developed thermal gradients along each arm, caused by outward heat transfer to the surrounding supercooled melt. The tangential component of the thermal gradient caused by the transport field is unrelated to its capillarity-mediated gradient, but adds a nearly uniform amount to the gradient near the tip. Comparison of Mullis's dynamic flux data with capillary heat fluxes calculated from Eq. (6) for a parabola requires adding a constant to the capillary-mediated component for the parabola. The flux component caused by capillarity is exactly zero at a symmetric tip, so Mullis's flux value of -15 at the dendrite tip, $x/\rho_a = 0$, is the value of the 'extraneous' transport component to be added. In addition, the ratio of the parabolic tip radius to the product of its capillary length, λ, with the (unknown) interface conductivity, $\lambda_c \times K_{int}$ are matched to equate the length scales of the dendrite and the parabola, and the vertical scale factor for the parabola's flux. The flux measured on a phase-field simulated dendrite, Fig. 4(left), are consistent with the capillary-mediated tangential flux magnitude calculated analytically for an ideal parabola, Fig. 4(right). As the form of the tangential interfacial flux is extremely sensitive to the strength of the anisotropy and the shape, the consistency shown provides a reasonably stringent comparison between phase field numerics and bias-field analytics.

Fig. 5a–c contains the relevant interfacial thermodynamic fields calculated analytically for a smooth parabola. These include: (a) the GTH thermo-potential, $\vartheta(x/\rho)$, (b) the magnitude of the dimensionless tangential flux, $\Phi(x/\rho)$, and (c) the bias field energy rate, $\mathcal{B}(x/\rho)$, all of which are plotted in Fig. 5 for various strengths of 4-fold crystalline anisotropy, ϵ_4, in 2-D given by Eq. (20). These dimensionless fields were calculated from Eqs. (2), (6), and (21), respectively.

Fig. 5c shows specifically that where $\mathcal{B} > 0$, the bias field adds capillary energy and slows the interface during crystal growth. Also, where $\mathcal{B} < 0$, the bias field withdraws energy and accelerates the interface during crystal growth. We note further in Fig. 5a that the GTH thermo-potential for a parabola becomes distinctly *non-monotone* as the tip is approached, provided that $\epsilon_4 \ge 1/95 \approx 0.0105$. Again, Mullis [66] verified the prediction of non-monotone interface thermo-potentials for a 'crystalline' parabola with 3% 4-fold anisotropy. He then showed that the dynamic shape evolved using phase-field avoids non-monotone potential distributions by developing some subtle curvature changes near its tip. The full explanation for this interesting observation of interfaces avoiding non-monotone potential distributions (which in turn affect the form of the bias field) requires further study before concluding that this might be a general dynamic response for anisotropic crystals.

Nevertheless, as revealed in Fig. 5a and c, a monotone GTH thermo-potential and the corresponding bias field curves for an ideal parabola predict pattern changes with $\epsilon_4 \le 1/95$, for which only one (pair) of Laplace points appears in the $\mathcal{B}$ – field (i.e., only a single pair of sign-reversing perturbations occurs). For parabolic interfaces with $\epsilon_4 \ge 1/95$, non-monotone GTH thermo-potentials occur and an additional pair of Laplace points for the $\mathcal{B}$-field appear extremely close to the tip. When $\epsilon_4 = 1/95$, the $\mathcal{B}$-field marginally retains a second root, poised exactly at the tip, $x/\rho = 0$. Thus, in 2-D, a 4-fold energy anisotropy of about 1% separates sign-reversal behavior for parabolas into two cases: (1) those with a single pair of Laplace points well aft of the tip, and (2) those with an additional pair of Laplace points extremely close to the tip. These differences might affect subsequent speed perturbations and influence shape modulation and overall pattern development for systems with 'low anisotropy' (i.e., $\epsilon_4 < 1\%$), compared to those with 'high anisotropy' ($\epsilon_4 > 1\%$). The bias-field analysis clearly helps quantify what values of ϵ_4 actually constitute 'high' and 'low' energy density anisotropies. Additional study is needed to elucidate more fully the quantitative influences of anisotropy on details of dendritic pattern evolution.
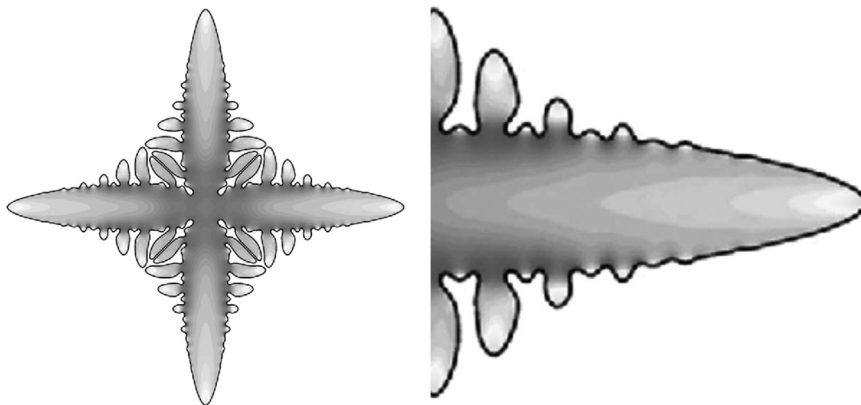

Fig. 3. Left Panel: Phase-field simulation solved over the full 2-D computational domain, φ: $[0, 2\pi]$. Calculations employed an implicit, multigrid solver that minimizes noise over all wavelengths, modified with a 4th-order accurate spatial discretization scheme, using a 17-point finite difference stencil. Four-fold anisotropy with medium strength, $\epsilon_4 = 0.02$, is imposed on an initially circular 'nucleus'. This simulation reveals a robust, perfectly 4-fold symmetric, branching pattern, stimulated by some type of 'perturbations' constrained by crystallographic symmetry. Right Panel: Detail of the right-hand dendrite arm. The interface exhibits a series of smaller, perfectly mirror-symmetric modulations that remain recognizable at the smallest resolved scale. This result indicates the lack of significant noise affecting the symmetric interfacial oscillations. Gray-scale contours, best observed in the right panel, reveal complicated thermal gradients internal to the growing crystal. Original color image provided courtesy of Professor A.M. Mullis, University of Leeds, UK [65].
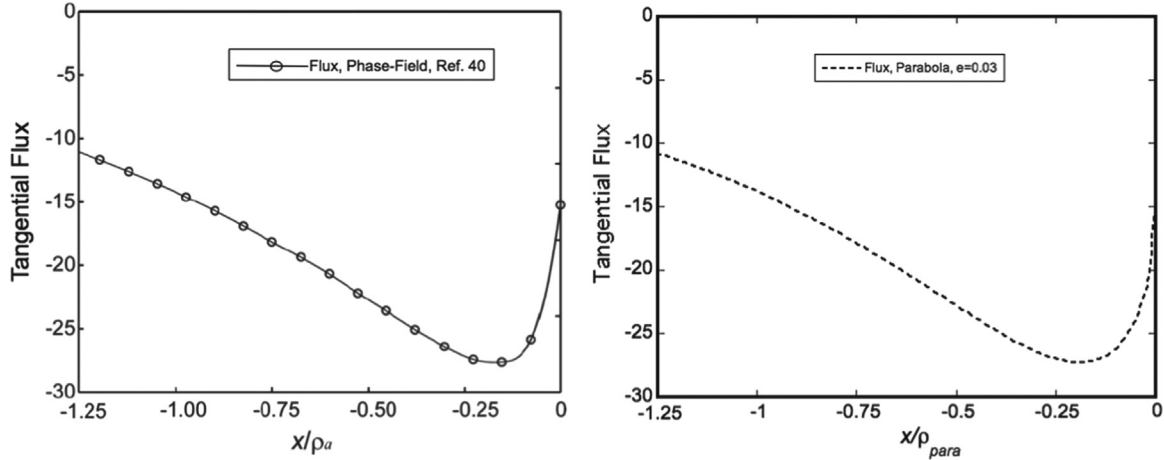
Fig. 4. Left panel: Tangential flux magnitudes reported by Mullis [66] along the phase-field isoline defining the interfacial tip region of a simulated dendrite tip, similar to the image shown in Fig. 3, right panel. The simulated solid–liquid interface supports 4-fold energy anisotropy with $\varepsilon_4 = 0.03$. Mullis confirmed the presence of small cyclic pulsations near the dendrite tip (see Fig. 8 in [66]). Right panel: Tangential flux magnitude, $\Phi(x/\rho_{para})$, calculated analytically for a smooth parabolic interface at local equilibrium, also supporting anisotropy with strength $\varepsilon_4 = 0.03$. The capillary-mediated flux, Eq. (6), from which the tangential flux was calculated does not include any contributions driven by gradients from the bulk transport fields responsible for net growth. Given that the capillary-mediated flux calculated analytically is exactly zero at the parabola's tip, $x/\rho_{para} = 0$, a constant flux of -15 units was added to Eq. (6) to match Mullis's flux value at $x/\rho_a = 0$, allowing comparison with the interfacial flux reported along the simulated dendrite. Note too, that the forms of both the interface flux and its bias-field energy are extremely sensitive to the value of ε_4 for a parabolic interface. (Cf. the flux here with the curves plotted in Fig. 5b at different anisotropy strengths.).

6.2.2. Sharp interface modeling

A decade prior to Mullis's precision phase-field results, an accurate integral equation solver was developed by Lowengrub et al. [67–69] for solving the phase-field equations in the 'sharp-interface' limit. Their dynamic model solves Laplace's equation in the bulk phases and uses dense distributions of Greens function sources and dipoles along a prescribed interface to track pattern evolution in fluids and crystals. Li and Lowengrub's solver was, to the author's knowledge, the first one capable of detailing complete evolution of complex diffusion-limited patterns with sharp interfaces from simple initial conditions. Their dynamic solver provided the first simulation data that confirmed and revealed what the author believes is the presence of the capillary bias-field, as their simulations show intrinsic interface speed perturbations, shape modulations, and allows separation of their subsequent amplification by the imposed external field. Their numerical code, moreover, uses a mathematical transformation that accurately subtracts any net volume or overall area changes caused by phase transformation in $\mathbb{R}^3$ or $\mathbb{R}^2$, respectively [69]. A few of our earliest observations [70] of diffusion-limited pattern formation are reviewed next, but now discussed on the basis of a deeper understanding of the responsible thermodynamic mechanism.

6.2.3. Circular disk crystal

Calculating the initial bias field and simulating the subsequent shape dynamics at a interface are easier in 2-D for a starting shape based on smooth circular disk crystals that exhibits interface energy anisotropy, but initially lacks curvature variations on the interface. Eliminating the starting shape's curvature variations eliminates all derivatives of the initial curvature with respect to normal angle, $\kappa(\varphi, t = 0) = \text{const}$. Thus, one finds that the *initial* $\mathfrak{B}$-field reduces to a simpler mathematical form. Specifically, only the first term in Eq. (20) survives for a circle, providing an exact expression for the capillary bias-field at time zero that acts on a circular interface with 4-fold anisotropy. One obtains for this special case

$$\mathfrak{B}(\varphi, 0) = -\left(\frac{\gamma_{\varphi,\varphi} + \gamma_{\varphi,\varphi,\varphi,\varphi}}{\gamma_0} \right) \hat{\kappa}^3. \tag{26}$$

6.3. Perturbations on anisotropic circular 'seeds'

A circular interface with initial radius R is subject to 4-fold energy anisotropy of the following harmonic form:

$$\frac{\gamma(\varphi)}{\gamma_0} = 1 + \epsilon_4 \cos(4\varphi). \tag{27}$$

Here the coefficient ϵ_4 in Eq. (27) again denotes the strength of the anisotropy of energy density. The starting interface may be described parametrically as $x = R \sin(\varphi)$, $y = R \cos(\varphi)$, with initially uniform dimensionless curvature, $\hat{\kappa} = R\kappa$. The bias field, Eq. (26), is evaluated with anisotropy condition (27), by inserting the 2nd and 4th angular derivatives of the energy density round the circular 'seed'. The initial perturbation spectrum is prescribed by the bias field, $\mathfrak{B}(\varphi, 0)$, with the net radial changes from melting or growth adjusted through a uniform scale factor, $a = 1$, applied sequentially with the initial perturbations to the starting radius, R. See Fig. 6.

One obtains the dimensionless bias field for a circular disk crystal of unit curvature, $1/a = 1$ by inserting the derivatives of the energy anisotropy into Eq. (26), giving the result

$$\mathfrak{B}(\varphi, 0) = -240\epsilon_4 \cos(4\varphi). \tag{28}$$

The initial bias field on a circle, Eq. (28), exhibits multiple roots, consisting of 8 Laplace points, about which capillary energy rates change sign, inducing opposing speed perturbations. The zeros occur round a circular interface at 8 locations $\varphi^\star = \frac{1}{8}\left(\pm\pi + 4\pi j \right)$, where the indices $j = 0, 1, 2,$ and 3, delineate four interface regions of retarded growth (or enhanced melting) separated by four adjacent regions of enhanced growth (or retarded melting). Fig. 6 provides graphical comparisons calculated from Eq. (28) of initial shape changes imposed by capillary energy on growing (left panel) and melting (right panel) anisotropic disk crystals. The small but opposite curvature changes occurring adjacent to the 8 Laplace points are explained in this figure, and account completely for its early evolution and shape modulation.

6.3.1. Dynamic shape changes

Evolution of an anisotropic circular 'seed' of a dilute metallic alloy solidifying into its melt was studied numerically by Reuther and Rettenmayr [71,72]. These investigators used the diffusion
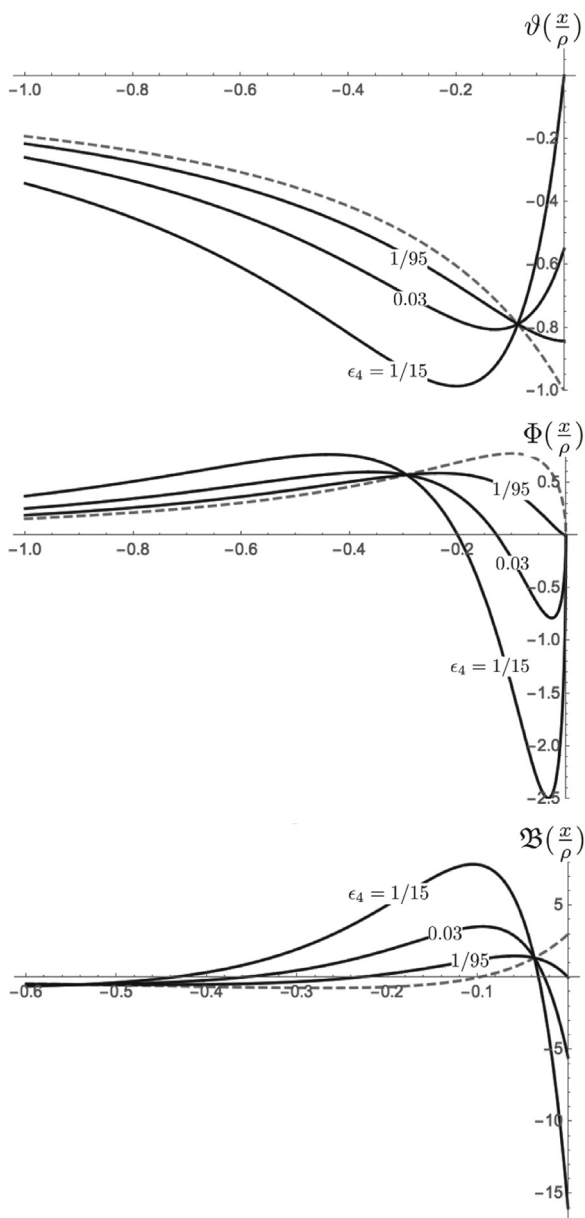
Fig. 5. Capillary-mediated interfacial fields for the parabola, $(y/\rho)^2 = -1/8(x/\rho)$, where $\rho = a/2$ is the parabolic tip radius. Plot (a) GTH thermo-potential, $\vartheta(x/\rho)$; Plots (b) tangential flux magnitude, $\Phi(x/\rho)$; Plot (c) scalar bias field, $\mathfrak{B}(x/\rho)$. Dashed curves are field plots for *isotropic* interfaces, where $\epsilon_4 = 0$. Bias field plots are shown in a smaller neighborhood near the tip ($-0.6 < x/\rho \leq 0$), and display strong sensitivity to the value chosen for the 4-fold anisotropy. The bias field provides a source of energy where $\mathfrak{B} > 0$, and an energy sink where $\mathfrak{B} < 0$. Capillary energy redistribution results in small speed perturbations and shape modulations adjacent to Laplace points where each curve crosses the x/ρ – axis from the $-x/\rho$ direction. A second pair of Laplace point occurs extremely close to the tip for 4-fold anisotropies $\epsilon_4 \geq 1/95$.

approximation method to solve Laplace's equation combined with meshless front tracking to eliminate artifacts induced by false grid anisotropy. Their dynamic solver follows diffusion-limited pattern formation through front tracking with energy conservation. Their numerical results illustrate how net crystal growth (accompanying what the present author believes are shape changes induced by bias-field perturbations) evolves toward branched morphologies in a low-noise 2-D environment. These authors calibrated their numerical simulations against several well-known 1-D analytic solutions and 2-D numerical solutions for classical moving boundary problems, which include the time-dependent

solidification of an infinitely long, orthogonal, corner heat sink [73–75]. Excellent correspondence was reported between those published solutions with their dynamic front-tracking results.

Comparison is provided in Fig. 7 of Reuther and Rettenmayr's dynamical contours for an anisotropic circular 'seed' with those calculated from the initial bias-field perturbations for the circular anisotropic seed. The contours displayed in the right panel were determined by applying for each time step the *unchanged* initial bias-field perturbations given by Eq. (28). Considering that the 8 initial Laplace points remained unadjusted with the changing interface shape after each time step, the correspondences between analytically calculated and the simulated contours found over the first 1.2 ms of crystal growth appear reasonably close. However, as the crystal growth time exceeded 1.2 ms, pairs of transverse bumps developed behind the four advancing cruciform tips. The initial bias-field, with only 8 Laplace points, of course, no longer can serve as an accurate representation of the observed interface speed perturbations. In fact, 16 additional Laplace points are needed to account for the additional interface inflections that developed after 1.2 ms of unstable growth. These additional Laplace points cannot be determined analytically, but, in the author's opinion, occurred spontaneously in the course of this dynamic simulation.

6.3.2. Interface inflection and Laplace points

In 2011, Li and Lowengrub provided the author dynamic simulations of the evolution of two smooth semi-elliptical crystal–melt interfaces growing into their supercooled pure melts [76]. The initial seeds had the analytical form, $y = \pm \frac{B}{A}\sqrt{1 - x^2}$, with aspect ratios (major-to-minor axial ratios) of $A/B = 2$ and $A/B = 3$. The tips of these semi-ellipses were located, respectively, at $x_{tip} = \pm 2$ and $x_{tip} = \pm 3$, and their mid-planes were located precisely at $x_{mid} = 0$. These interfaces were subject to 4-fold anisotropy with $\epsilon_4 = 0.005$. Video frames taken from relatively early stages of pattern development (the first 50 frames) of Li and Lowengrub's dynamic simulation were measured to locate the times and positions of detectable interface inflections that follow the evolving 'elliptical' tips. Each inflection observed in the simulation corresponds theoretically to a Laplace point, $X^*(t)$, where the time-dependent bias-field reverses sign and stimulates inflection on the interface. The positions for inflections on the smooth starting ellipses at $t=0$ are visually undetectable on the first few video frames, as their initial perturbations are initially too small to measure directly. One must await some amplification to occur by the specified external transport field. Thus, the positions of the initial Laplace points, $X^*(0)$, on the smooth ellipses were determined by backward extrapolation to frame '0'. This was accomplished by regressing all the dynamically observed inflection-coordinates observed on frames 5–46 of the evolved interface patterns from the semi-ellipse with $A/B = 2$, and from frames 2–36 of the evolved patterns from the semi-ellipse with $A/B = 3$. The dynamically observed regressions obtained by plotting the positions of inflections are shown in Fig. 8. Using limited time ranges of the two video sequences allowed measurement of sequential pairs of interface perturbations occurring behind the advancing tip. Linear regression of the video data ($\times$ - and •-symbols) capture precisely the statistical ordinate intercepts, M_0, listed on the figure, which locate where perturbations started at zero time on the original smooth analytically-specified ellipses. The statistical intercepts extracted by linear regression agree within $\pm 0.2\%$, when compared with the positions calculated exactly from Eq. (21) of the *initial* bias-field Laplace points (□-symbols), viz., $X^*_{2:1}$ and $X^*_{3:1}$, the values for which are listed to four decimal places along the ordinate.

6.3.3. Long-term pattern evolution

Lowengrub and Li also investigated the long-term dynamic shape changes of a 4-fold anisotropic circle. They evolved a circular crystallite for growth times well beyond the early inflections
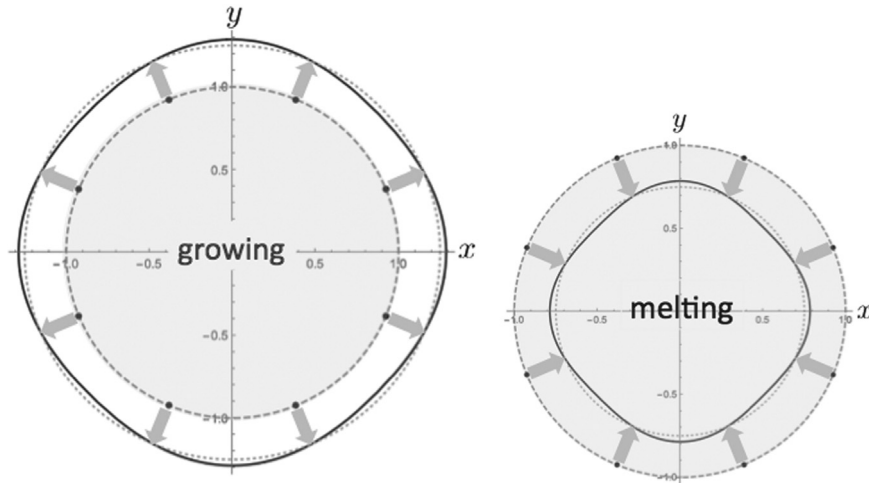
Fig. 6. Local bias field dynamics affecting short-time shape changes on circular disk 'crystals'. Left panel: Crystal growth into cooled melt ($T < T_m$) surrounding an initially circular disk (dashed inner circle with $R=1$) supporting 4-fold energy anisotropy ($\epsilon_4 = 0.01$). Average radius after growth increment increases by 25% is $\langle R \rangle = 5/4$. Arrows point in growth directions from initial Laplace points (black dots), where $\mathfrak{B}(\varphi, 0)$ changes sign. Arrows terminate on the evolved interface (larger non-circular contour) where the local radius of curvature matches the growing crystal's average radius, as specified by the outer dotted circle. Intersections between the dotted circle and the crystal contour denote sectors where curvatures, $\kappa(\varphi, t > 0)$, oscillate from larger to smaller than the average curvature, $\langle \kappa \rangle = 4/5$, of the enlarged growing crystal. Right panel: Crystal melting in a heated melt ($T > T_m$) surrounding an initially identical circular disk crystal (dashed outer circle with $R=1$). Average radius after melting decreases 25% to $\langle R \rangle = 3/4$. Arrows point in melting directions from each Laplace point (black dots) where $\mathfrak{B}(\varphi, 0)$ changes sign. Arrows terminate on the non-circular evolved interface (smaller crystal contour) where the local radius matches its average radius specified by the inner dotted circle. Intersections between the dotted circle and the crystal contour denote interface sectors where curvatures, $\kappa(\varphi, t > 0)$, oscillate from larger to smaller than the average, $\langle \kappa \rangle = 4/3$, of the partially melted crystal.
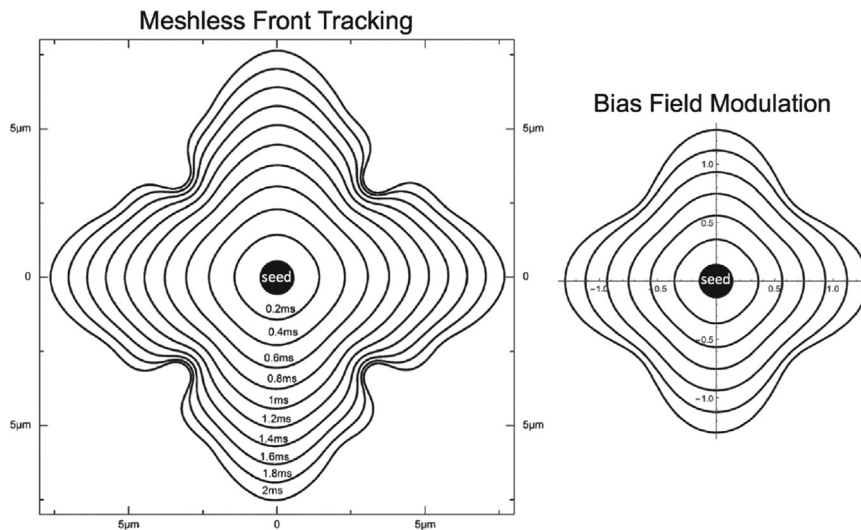

Fig. 7. Left panel: Dynamic meshless front tracking of a circular seed crystal growing with 4-fold anisotropy, $\epsilon_4 = 0.01$. Contours simulated at progressive time intervals up to 2 ms of physical growth time using the diffusive approximation method as simulated by Reuther and Rettenmayr. Time and distance scales for the solid–liquid contours correspond to thermophysical constants chosen for the crystal and melt phases [72]. Right panel: Sequence of growth contours calculated analytically for the identical starting 'seed' using bias-field shape modulations. 8 initial Laplace points, located at fixed positions around the starting seed, yield good approximations to the dynamical front tracking results up to about 1 ms of physical growth time. Beyond 1ms, front tracking dynamics show that secondary bumps develop on the four arms, initiating 16 additional dynamical inflections along the interface. These correspond to 16 additional Laplace points that cannot be determined analytically.

appearing on the two semi-ellipses shown in Fig. 8, which could still be estimated analytically by using initial bias-field perturbations, or even those shown using front tracking in Fig. 7. Lowengrub and Li, as already mentioned, used a high-precision Laplace equation solver with all energy exchanges associated with the interface and its surroundings tracked accurately [67–69]. The growing crystal was subject to a far-field thermal condition specified by a boundary temperature or a far-field flux.

The dynamic patterns produced with this numerical code were also subject to a mathematical transformation that maintains a fixed number of pixels to comprise the evolving pattern in 2-D, or a fixed number of voxels in 3-D. Their model is ideal for exposing

modulations stimulated by what we claim is the capillary bias field. Dynamic results for the case of an initially circular interface subject to 4-fold anisotropy evolved over a long period, sufficient to approach a steady dendritic tip form, are shown in Fig. 9. Here one observes the full range of spontaneously-evolved patterns that derive from an anisotropic circular disk crystal growing into its surrounding melt. The series of dynamic shapes is continually modified by sequences of interface inflections and branching, until what appears to be a limit cycle develops, where the pattern synchronizes into a classical dendritic form. At this advanced point in the pattern's development, any semblance of its initially smooth circular shape no longer remains. The observed sequence of
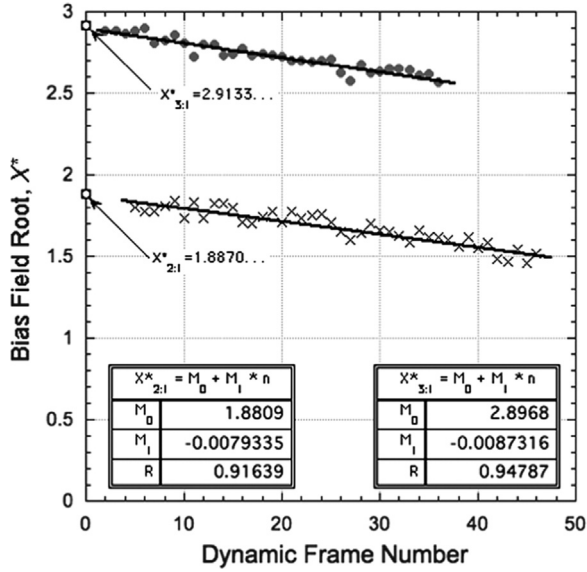
Fig. 8. Coordinate locations of *analytic* Laplace points ($X^\star_{3:1}$ and $X^\star_{2:1}$) versus *observed* dynamic interface inflections ($\times$, $\bullet$, data) versus time, or dynamic frame number. Laplace points locate theoretical positions where interface inflections initiate behind the advancing tips of two semi-elliptical protrusions, $y = \pm \frac{B}{A}\sqrt{1 - x^2}$, with eccentricities $A/B = 2:1$, ($\times$ symbols), and $A/B = 3:1$, ($\bullet$ symbols). Each starting semi-ellipse is 4-fold anisotropic, with $\epsilon_4 = 0.005$. Both data sets have regression coefficients $R > 0.9$, yielding intercepts, M_0, for the x-coordinates of the initial perturbations. Regressed pattern measurements and analytical predictions for the initial Laplace points for $X^\star_{3:1}$ and $X^\star_{2:1}$ agree within $\pm 0.2\%$. See $\square$-symbols located on the ordinate that were calculated from Eq. (21). Video simulation data provided through the courtesy of Lowengrub and Li [76].

pattern changes follow, in the author's opinion, the number and location of discrete denumerable inflections that are induced dynamically by Laplace points in the bias field.

6.4. Isotropic systems

Although the intent here is to explain the origin of diffusion-limited shape change in crystalline microstructures, the application of bias field thermodynamics also extends to interfaces with non-uniform curvature for which the energy density is either isotropic or exhibits extremely weak anisotropy. In the limit of perfect isotropy, i.e., interface energy density ($\gamma(\varphi) = \gamma_0$) that is independent of orientation, the crystal–melt bias field, Eq. (19), reduces to the following non-linear 4th-order form that depends *only* on the interface curvature and its first and second derivatives

$$B(\varphi) = -\left(\frac{K_{int}\gamma_0 \Omega}{\Delta S_f} \right)\left[\kappa_{\varphi\varphi}\kappa^2(\varphi) + \kappa_\varphi^2 \kappa(\varphi) \right]. \tag{29}$$

The Laplace points of the bias field, $\varphi^\star$, where $B(\varphi^\star) = 0$, along an energetically *isotropic interface* occur where interface inflections (opposing curvature changes) can eventually initiate. The orientations and locations, $\varphi^\star$, of bias-field zeros correspond to the condition that the interfacial curvature and its first and second angular derivatives satisfy the non-linear differential equation

$$\kappa_{\varphi\varphi} + \frac{\kappa_\varphi^2}{\kappa(\varphi^\star)} = 0, \quad (\kappa(\varphi^\star) \neq 0). \tag{30}$$

Simulations for such energetically *isotropic* interfaces in 2-D generally evolve toward extremely complex interfacial patterns that resemble 'seaweed', 'coral', or other natural growth forms. The author believes that highly complicated patterns form between isotropic phases from the creation of an 'avalanche' of Laplace points, where sufficient crystalline symmetry is no longer available to organize and delimit the interface inflections, invaginations and

splittings that subsequently take place. The untrammeled multiplication and release of Laplace points that are generated during evolution of isotropic interfacial patterns does indeed appear chaotic, 'random', and seemingly 'unpredictable'; but, in fact, such patterns remain fully deterministic. Moreover, it appears that isotropic patterns induce dynamics that display extreme sensitivity to initial conditions, where the lack of anisotropy promotes uninhibited, omnidirectional growth, exhibiting profuse irregular branching and splittings of an evolving interface.

Fig. 10 (left panel) shows an example of a complex diffusion-limited radial pattern, evolved from an initially smooth, perfectly isotropic, slightly distorted, trefoil shape. This pattern was also simulated by Lowengrub and Li [69]. The increasingly dense sequence of autogenous Laplace points perturbs the unstable isotropic interface, producing a chaotic-looking pattern of what appears as ever-increasing complexity. There remains little doubt that without the organizing effects of crystalline anisotropy to constrain diffusion-limited pattern evolution, any closed starting shapes in 2-D, or 3-D, eventually evolve by a myriad of omnidirectional forking and branching, producing in turn an almost endless number of Laplace points in 2-D or Laplace lines in 3-D. More study on the limits and characteristics of such 'random' fluid-fluid patterns based on bias-field dynamics is appropriate for future investigations.

Fig. 10 (right panel) shows an example of a highly disorganized diffusion-limited pattern created by simulated directional crystallization of a pair of misoriented grains (black and gray). The solid–liquid interfaces for both crystals are weakly 4-fold anisotropic, with $\epsilon_4 = 0.001$. These grains share a vertical boundary with the black grain tilted $30°$ from the preferred orientation of the gray grain. One observes in the video sequence that the grain boundary and the solid–liquid interface, upon equilibrating, immediately form a localized grain boundary groove, from which a pair of slender finger-like protrusions (black on the left, gray on the right) advance into the melt. These initial protrusions then commence to split and fork repeatedly, and quickly develop into a highly ramified structure containing poorly-defined irregular dendritic forms. The original dynamic sequence from which this quasi-isotropic pattern was obtained was simulated by Ankit and Nestler [77], who used multiphase-field numerics based on the grand-chemical-potential model with periodic (no-flux) boundary conditions applied to the left and right borders of the computational box [78,79].

Lastly, mathematical descriptions of steady-state cellular shapes in both 2-D and 3-D were derived for incompressible penetration of two fluids by Saffman and Taylor [80]. Saffman and Taylor compared their theoretical cell shapes with experimentally observed patterns obtained with two interpenetrating insoluble fluids in Hele-Shaw cells. Their analytic 'viscous fingering' profiles have also been adopted by several investigators attempting to describe the dynamics of steady-state cellular crystalline patterns that occur commonly in directional crystallization of dilute alloys [81,82]. You, Wang, and Wang recently investigated the stability of simulated cellular substructures in a directionally crystallized dilute binary alloy modeled at steady-state [82]. You et al. chose to evolve dynamically a smooth Saffman–Taylor finger shape and found, using phase-field simulations, that the critical ratio of the cellular tip radius to finger width, α, where instability occurs is $\alpha \approx 0.39$. You et al. then compared their numerical results against the analytical result provided by bias-field perturbation analysis, which gives the exact value for $\alpha = \sqrt{3/2}/\pi = 0.3899\ldots$ These investigators reported quantitative agreement between their pattern formation results on cellular interface stability using phase-field simulation and exact predictions based on bias-field analysis. Moreover, You et al. also concluded that the observed dynamic pattern change (cell splitting instability) is stimulated by release of capillary-mediated interfacial energy [82].
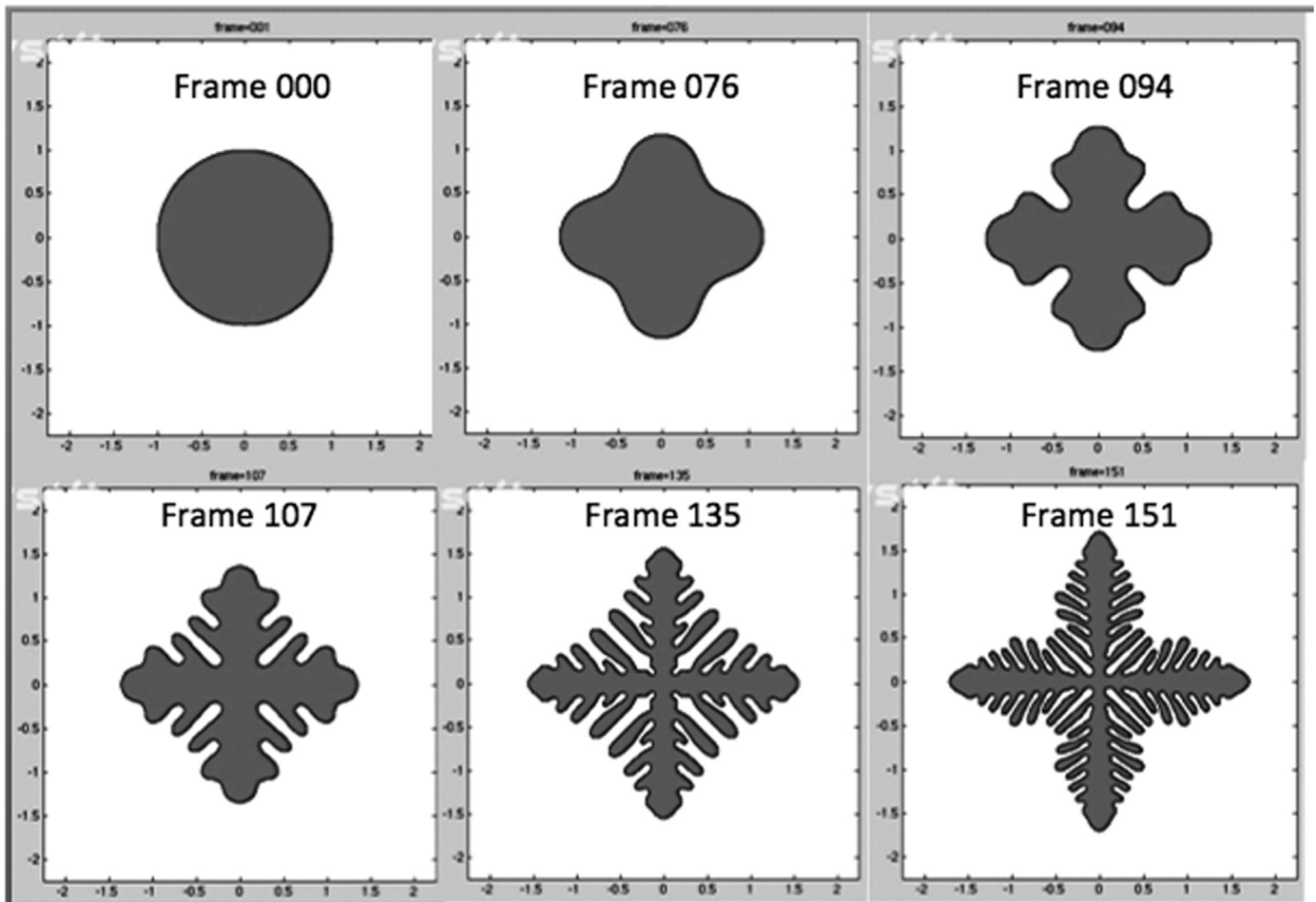
Fig. 9. Long-term growth of a circular crystal, subject to 4-fold anisotropy, $\epsilon_4 = 0.005$. Frames extracted from a numerical simulation that accurately solves integral equations based on dense distributions of interfacial Greens functions. This simulation is comparable to phase-field numerics in the limit of a sharp interface. Frame 000 shows the starting smooth 'disk crystal.' Frame 076, displays retarded and accelerated regions that correspond with the outer analytically modulated contour shown in Fig. 7, right panel. Frame 094 shows the evolved interface after 8 lateral bumps appear in the pattern, stimulated by 16 additional dynamical Laplace points that cause inflections along the four $\langle 10 \rangle$ primary protrusions. The lower three panels suggest how continued repetition and synchronization of interface inflections and branching at hundreds of perfectly symmetric dynamical Laplace points eventually produce a limit cycle that leads to a classical dendritic form (frame 151). Area of dark pixels remains constant in each frame through benefit of a mathematical transformation that eliminates 'crystalline' pixels added by net growth. This simulation develops an increasingly complex symmetric pattern within a fixed computational box, exposing the growth of multiple generations of autogenous perturbations. Simulation provided through the courtesy of Lowengrub and Li [76].
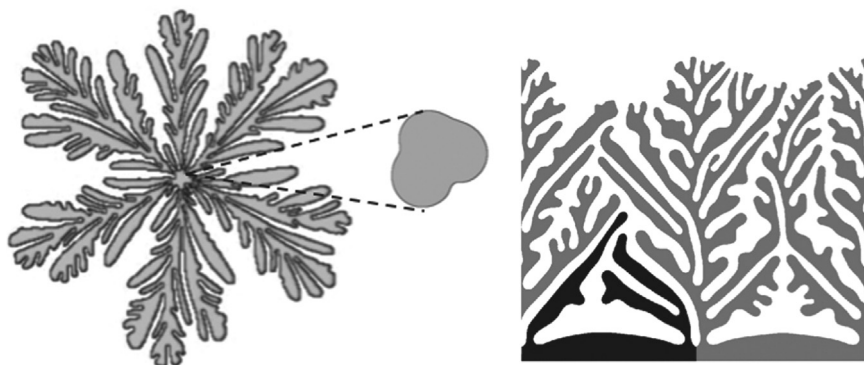

Fig. 10. Left panel: Radially grown 'seaweed' pattern simulated from the growth of a slightly distorted, trefoil 'bubble' (see insert) with constant, i.e., *isotropic*, interface energy. Rapid multiplication of Laplace points, unconstrained by crystalline anisotropy ($\epsilon = 0$) results in a seemingly random, chaotic pattern, lacking symmetry or directionality. The appearance of interface inflections, invaginations, tip splittings, and branchings are, nevertheless, deterministic. This pattern is an example of what occurs when the bias field operates in an environment where extreme sensitivity to initial conditions prevails. Simulation from a low-noise dynamic solver provided through the courtesy of Lowengrub and Li [76]. Right panel: Multiphase-field simulation in 2-D of directional crystallization from an initially flat 'bi-crystal seed', containing a vertical 30° mis-orientation boundary at its mid-point. The solid–liquid interfaces for both the black and gray phases are weakly anisotropic, as $\epsilon_4 = 0.001$. Periodic boundary conditions apply at the right and left borders, and the numerical domain size is 1000×1000. Upon equilibration with the melt, the grain boundary initiates a small groove on the solid–liquid interface, from which two finger-like protuberances extend upwards into the melt. Then, the fingers fork, split, and branch into a complex highly ramified microstructural pattern. Directional crystallization appears irregularly 'organic', even chaotic, but this pattern is both repeatable and deterministic. The bias-field, unconstrained by a significant level of anisotropy, generates numerous Laplace points that inflect the interface at an ever increasing number of locations. Image extracted from a multiphase-field simulation video, courtesy of Dr. Kumar Ankit and Prof. Britta Nestler, KIT, Karlsruhe, Germany [77].
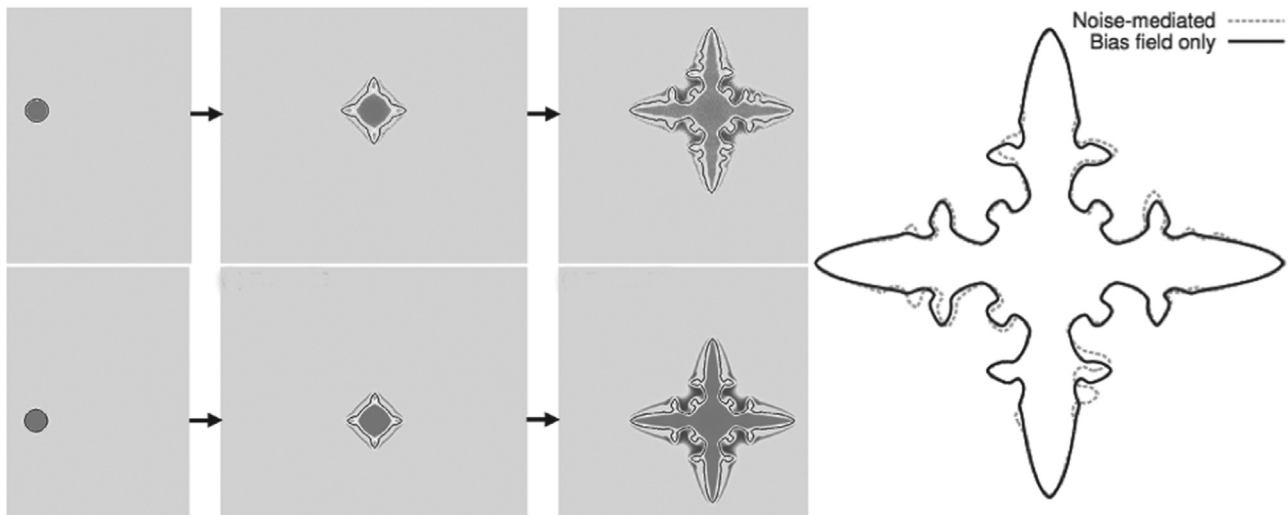
Fig. 11. Direct comparison between low-noise, and noise-added, multiphase-field pattern simulations. Lower video panels selected from a low-noise multiphase-field simulation. Upper video panels simulated under identical phase-field conditions, except for inclusion of noise-augmentation. Both pattern sequences start with identical circular 'seed' crystals with initial radius $R = 15\Delta x$, where Δx is the computational grid spacing. Energy anisotropy is 4-fold for both simulations, with $\epsilon_4 = 0.05$. Injection of random noise accelerates the overall rate of growth, and introduces minor distortions into the pattern that break the perfect symmetry established by what the author believes are capillarity-mediated perturbations. Right detail consists of two pattern overlays comparing the low-noise (solid black) isoline with the noise-augmented (gray dotted) isoline, chosen at the same tip separation. Only minor differences appear with noise injection from the basic pattern. Simulation images courtesy of Dr. Kumar Ankit and Prof. Britta Nestler, KIT, Karlsruhe, Germany [77].

6.5. Effects of added noise

Ankit and Nestler [77] recently checked on the specific influences of random noise additions during pattern evolution using multiphase-field numerics. Fig. 11 compares the evolution of a smooth 4-fold anisotropic circular 'crystal' into a branched cruciform pattern, with and without added noise. The lower 3-panel sequence of video frames shows pattern evolution devoid of added random noise, whereas the upper 3-panel sequence includes appreciable noise augmentation. Little difference is noticeable between the two simulations, except that for equal evolution time the noise-augmented patterns in the second and third upper video frames appear slightly larger (more evolved) than do their counterparts simulated below without added noise. The isolines of these simulated patterns are compared directly in the enlarged detail inserted at the right of Fig. 11. The images (solid black isoline) grow as perfectly symmetric 4-fold patterns over all orientation space, indicating no detectable effects from randomness. This result indicates that the observed pattern in 2-D is derived from perturbations that are linked directly to the imposed crystallographic symmetry, as is the capillary-mediated bias field. The noise-augmented images (gray dotted isoline) show the presence of minor irregularities that break strict 4-fold symmetry, and even stimulate extra branches in a few locations. Although no quantitative conclusions can be drawn from this single test, these data support the idea that the basic character of diffusion-limited patterns may evolve without benefit of selective noise amplification.

7. Conclusions

1. Observations of ellipsoidal crystallites melting in microgravity under pure diffusive heat flow allowed the first quantitative measurement of their axial ratios as melting progressed and their size was reduced. Those experiments suggested that capillarity may induce major shape changes during active phase transformation. The action of capillarity on growing crystals is found to be even more dramatic, insofar as capillary-mediation also induces branching, invagination, and splitting that increase pattern complexity. Analyses presented here show that capillary fields in crystal–melt systems are of intrinsic thermodynamic origin, and their appearance and action during crystal growth or melting are the results of energy conservation and the dynamics of interface curvature change.

2. Energy conservation (Leibniz–Reynolds theorem) indicates that a unary crystal–melt interface evolving at local equilibrium has at least two independent energy sources: (1) robust release or absorption of latent heat from phase transformation, and (2) divergence of capillary-mediated tangential heat flux. The latter is a relatively weak source/sink of thermal energy—termed the 'bias field'—which depends sensitively on system size, shape, and anisotropy. Vector field theory shows that the bias field is a net-zero source/sink of energy. Locally, however, the two independent source terms—latent heat and the bias field—couple on brief time intervals, and perturb the interface over mesoscopic scales (circa 100 nm to 1 mm). The algebraic sum at each interfacial point of source terms must continually balance the energy transported via long-range, quasi-static gradients. On short time scales such macro-gradients conduct essentially *fixed* rates of thermal energy to and from the surrounding phases. The interactions between fast acting microscopic sources and relatively slow changing transport gradients dynamically provide interface speed perturbations and shape modulation during crystal growth.

3. Interfaces stimulated by capillarity in 2-D can inflect and 'curl' at isolated Laplace points, where the bias field energy rate reverses sign. Inflections can arise because the curvatures of the adjoining interface shift in opposite directions about zero in response to the bias field. This results in an unusual, but classical, Le Chatelier–Braun thermodynamic response. The scalar bias field, moreover, is proved to average toward zero at large macroscopic length scales, masking its presence by leaving the system's *overall* transformation rate unchanged. Nonetheless, the bias field is capable of locally perturbing the interface speed on smaller length scales where capillarity becomes significant, giving rise to intrinsically-driven interfacial modulations in the

form of bumps, invaginations, and splittings. The bias field itself is a non-stochastic scalar energy field of thermodynamic origin capable of providing self-induced (autogenous) perturbations independent of any extrinsic signals or noise.

4. Comparison of analytically derived interface patterns with those from several thermodynamically consistent numerical models shows qualitatively congruent pattern predictions and yield quantitative details regarding specific pattern aspects such as their initiation at inflection points. Several comparisons, modeled dynamically by independent groups of investigators, indicate that capillary energies leading to interface perturbations are already fully accounted by thermodynamically consistent numerical models. These include different 'flavors' of phase field, level sets, and models designed for sharp interfaces using front tracking. The intrinsic pattern-forming mechanism of capillary-mediated interfacial heat fluxes therefore *need not be added to any accurate numerical model*, as such models already embody the physics for autogenous pattern evolution. Clearly, future attempts to control solidification substructures and crystal growth patterns at pattern-forming scales must rely on engineering approaches developed using relevant physics. Quantitative checks now indicate close agreement between the analytically-derived locations of bias-field Laplace points, where capillary-mediated energy rates reverse sign, and where corresponding interfacial inflection points are observed during simulations. In several recent tests conducted on smooth starting shapes by independent groups, and reported here, satisfactory agreement is found for both circular 'seed' crystals and protuberant shapes such as parabolas and semi-ellipses. Additionally, detailed measurements (e.g., Fig. 4) representative of important process details, such as the interface flux distribution during simulated growth of dendritic shapes show quantitative agreement when compared with analytically-derived tangential fluxes on comparable interface profiles supporting interfacial gradients in the GTH thermo-potential.

5. Diffusion-limited patterns stimulated by the capillary bias field in isotropic or weakly anisotropic systems show a propensity to produce an unconstrained 'avalanche' of Laplace points, wherein the interface inflects at many seemingly unrelated locations. These 'organic' growth patterns appear chaotic, but, in fact, they remain deterministic. The lack of energy anisotropy induces extreme sensitivity to initial conditions, which is a dynamical condition that suggests random, noisy behavior. This behavior might help explain dynamical patterns observed in Hele-Shaw cells, where viscous fingering is studied in fluid-fluid systems.

6. Under conditions not yet fully understood, bias-field Laplace points, or roots, synchronize with an advancing crystalline protuberance to form a limit cycle. This causes a pulsating train of inflections and periodic branches to develop just aft of the moving front, giving rise to classical dendritic forms. Capillary-mediated perturbations of the interface are fundamentally responsible for a variety of mesoscopic crystalline patterns found in both natural and man-made settings. These include hoar frost, and snowflakes—the iconic symbols of winter—as well as many mineral forms. Numerous diffusion-limited patterns arise spontaneously with important consequences in technical materials processing, including solidification of metals, alloy casting, welding and soldering, additive manufacturing, solution crystal growth, dissolution, sublimation, and electrocrystallization [83].

This article is dedicated to the memory of the author's colleague and friend, Dr. Robert J. Schaefer, who died on November 15, 2015. Bob Schaefer's abiding interests and life-long contributions to understanding crystalline patterns and solid-state microstructures, especially those of quasi-crystalline materials, will long be remembered by his loving family, close associates, and by the community of materials scientists and scholars who have been helped and inspired through his brilliant insights and careful experiments.

References

[1] J.W. Rutter, B. Chalmers, A prismatic substructure formed during solidification of metals, Can. J. Phys. 31 (1953) 15.

[2] C. Elbaum, B. Chalmers, The topography of solid–liquid interfaces of metal crystals growing from the melt, Can. J. Phys. 33 (1955) 196.

[3] W.A. Tiller, K.A. Jackson, J.W. Rutter, B. Chalmers, The redistribution of solute atoms during the solidification of metals, Acta Met. 1 (1953) 428.

[4] B. Chalmers, Melting and freezing, Inst. Met. Lecture, Trans. AIME 6, 1954, pp. 519.

[5] R.F. Sekerka, S.R. Coriell, G.B. McFadden, Morphological stability (Chapter 14), in: T. Nishinaga (Ed.), Handbook of Crystal Growth, 2nd edition, Elsevier, Amsterdam, 2015, pp. 595–630, vol. Ed..

[6] M.E. Glicksman, Dendritic growth (Chapter 16), in: T. Nishinaga (Ed.), Handbook of Crystal Growth, 2nd edition, Elsevier, Amsterdam, 2015, pp. 669–722, Vol. Ed..

[7] M. Asta, et al., Solidification microstructures and solid-state parallels: recent developments, future directions, Acta Mater. 57 (2009) 941–971.

[8] M.E Glicksman, Melting kinetics in microgravity, J. Phys. Conf. Ser. 327 (2011) 012001.

[9] M.E. Glicksman, Casting, in: ASM Handbook 15 ASM, Novelty OH, 2008, pp. 398–401.

[10] M.E. Glicksman, M.B. Koss, E.A. Winsa, Dendritic growth velocities in microgravity, Phys. Rev. Lett. 73 (1994) 573.

[11] M.B. Koss, M.E. Glicksman, E.A. Winsa, The chronology of a microgravity spaceflight experiment: IDGE, J. Met. 47 (1995) 49.

[12] C. Giummarra, J.C. LaCombe, M.B. Koss, J.E. Frei, A.O. Lupulescu, M.E. Glicksman, Sidebranch characteristics of pivalic acid dendrites grown under convection-free and diffuso-convective conditions, J. Cryst. Growth 274 (2005) 317–330.

[13] M.E. Glicksman, Melting kinetics in microgravity, J. Physics Conf. Ser. 327, Mater. Sci. Eng. 33, 2012, 1.

[14] A.M. Mullis, A phase-field model for the diffusive melting of isolated dendritic fragments, Metall. Mater. Trans. A 45 (2014) 3097–3102.

[15] M.E. Glicksman, S.R. Coriell, G.B. McFadden, Interaction of flows with the crystal–melt interface, Ann. Rev. Fluid Mech. 18 (1986) 307–335.

[16] G.B. McFadden, S.R. Coriell, M.E. Glicksman, M.E. Selleck, Instability of a Taylor–Couette flow interacting with a crystal–melt interface, Physico-Chem. Hydrodyn. 11 (1989) 387–409.

[17] G.B. McFadden, S.R. Coriell, B.T. Murray, M.E. Glicksman, M.E. Selleck, Effect of a crystal–melt interface on Taylor–vortex flow, Phys. of Fluids A 2 (1990) 700–705.

[18] C.J. Paradies, M.E. Glicksman, Flow interactions with dendritic mushy zones, in: S.H. Davis, H.E. Huppert, U. Müller, M.G. Worster (Eds.), Interactive Dynamics of Convection and Solidification, NATOASI Series E, Appl. Sci., vol. 219, 1992, pp. 81–95.

[19] G. McFadden, B. Murray, S. Coriell, M. Glicksman, M. Selleck, Effect of modulated Taylor–Couette flows on crystal–melt interfaces, in: M. Gurtin, G. McFadden (Eds.), On the Evolution of Phase Boundaries, IMA Volumes in Mathematics and Its Applications, vol. 43, Springer-Verlag Inc., New York, 1992, p. 81.

[20] G.B. McFadden, B.T. Murray, S.R. Coriell, M.E. Glicksman, M.E. Selleck, Effect of

a crystal–melt interface on Taylor-vortex flow with buoyancy, in: J.M. Chadam, H. Rasmussen (Eds.), Emerging Applications in Free Boundary Problems Pitman Research Notes in Mathematics, vol. 280, Longman Scientific & Technical, Harlow, Essex, UK, 1993, pp. 105–119.

[21] R.J. Braun, G.B. McFadden, B.T. Murray, S.R. Coriell, M.E. Glicksman, M. E. Selleck, Asymptotic behavior of modulated Taylor–Couette flows with a crystalline inner cylinder, Phys. Fluids A 5 (1993) 1891–1903.

[22] M.E. Glicksman, A. Lupulescu, M.B. Koss, Melting in microgravity, J. Thermophys. Heat Transf. Scope 17 (2002) 69.

[23] A. Lupulescu, M.E. Glicksman, M.B. Koss, Conduction-limited crystallite melting, J. Cryst. Growth 276 (2005) 549–565.

[24] M.E. Glicksman, A. Lupulescu, M.B. Koss, Capillary-mediated melting of ellipsoidal needle crystals, Int. Ser. Numer. Math. 154 (2006) 219–230.

[25] H.L. Le Châtelier, La loi de Le Châtelier, C. r. l'Acad. Sci. 99 (1884) 786.

[26] F.Z. Braun, Löslichkeit fester Körper und die den Vorgang begleitenden Volum- und Energieänderungen, Z. Phys. Chem. 1 (1887) 269.

[27] M.E. Glicksman, Mechanism of dendritic branching, Metall. Mater. Trans. A 43A (2012) 391–404.

[28] G. Wulff, Zur Frage der Geschwindigkeit des Wachsthums und der Auflösung der Krystallflächen, Z. Kristall. 34 (1901) 449530, http://dx.doi.org/10.1524/zkri.1901.34.1.449.

[29] B. Caroli, C. Caroli, B. Roulet, Non-equilibrium thermodynamics of the solidification problem, J. Cryst. Growth 66 (1984) 575.

[30] F. Davi, M.E. Gurtin, On the motion of a phase interface by surface diffusion, J. Appl. Math. Phys. 41 (1990) 782–811.

[31] C. Herring, in: W.E. Kingston (Ed.), Physics of Powder Metallurgy, McGraw-Hill, New York, NY, 1951, p. 143.

[32] C. Herring, The use of classical macroscopic concepts in surface-energy problems, in: R. Gomer, C.S. Smith (Eds.), Structure and Properties of Solid Surfaces, University of Chicago Press, Chicago, IL, 1953, pp. 5–72.

[33] C.A. Johnson, Generalization of the Gibbs–Thomson equation, Surf. Sci. 3 (1965) 429.

[34] P.M. Morse, H. Feshbach, The variational integral and the Euler equations, in: Methods of Theoretical Physics Part I. McGraw-Hill, New York, 1953, pp. 276–280.

[35] I.M. Gelfand, S.V. Fomin, Calculus of Variations Translated and Edited by R.A. Silverman, Dover Publications, Inc., Mineola, NY, 1991, pp. 42.

[36] A. Gray, E. Abbena, S. Salamon, Modern Differential Geometry (Chapter 13), 3rd ed., Chapman & Hall/CRC, Boca Raton, FL 2006, p. 385.

[37] G. Ehrlich, K. Stolt, Surface diffusion, Ann. Rev. Phys. Chem. 31 (1980) 603–637.

[38] M.E. Glicksman, Diffusion in Solids (Chapter 5), John Wiley & Sons Inc., New York 2000, p. 68.

[39] E.S. Machlin, Thermodynamic and Kinetics/Materials Science (Chapter VIII), Giro Press, Croton-on-Hudson, NY 1991, pp. 207–209.

[40] H.S. Carslaw, J.C. Jaeger, Conduction of Heat in Solids, 2nd ed., Clarendon Press, Oxford 1984, pp. 282–296.

[41] V. Alexiades, A.D. Solomon, Mathematical Modeling of Melting and Freezing Processes (Chapter 1), Hemisphere Publishing Corp., Washington, DC 1993, p. 21.

[42] J.J. Derby, A. Yeckel, Heat transfer analysis and design for bulk crystal growth, in: P. Rudolph (Ed.), Handbook of Crystal Growth, 2nd Edition, vol. IIb, Elsevier, Amsterdam, 2015, p. 808 (Chapter 20).

[43] S.H. Davis, Theory of Solidification, Cambridge University Press, Cambridge, 2001.

[44] O. Reynolds, Papers on Mechanical and Physical Subjects, vol. 3, Cambridge University Press, Cambridge 1903, pp. 12–13.

[45] L.G. Leal, Advanced Transport Phenomena: Fluid Mechanics and Convective Transport Processes, Cambridge University Press, Cambridge 2007, p. 23.

[46] C.C. Lin, L.A. Segel, Mathematics Applied to Deterministic Problems in the Natural Sciences, SIAM, New York 1995, pp. 484–485.

[47] B.J. Spencer, P.W. Voorhees, J. Tersoff, Morphological instability theory for strained alloy film growth: the effect of compositional stresses and species-dependent surface mobilities on ripple formation during epitaxial film deposition, Phys. Rev. B 64 (2001) 1–30.

[48] W.W. Mullins, Theory of thermal grooving, J. Appl. Phys. 28 (1957) 333–339.

[49] M.E. Glicksman, Diffusion in Solids (Chapter 21), John Wiley & Sons, Inc., New York 2000, pp. 359–375.

[50] J. Ye, C.V. Thompson, Mechanisms of complex morphological evolution during solid-state de-wetting of single-crystal nickel thin films, Appl. Phys. Lett. 97 (2010) 071904, http://dx.doi.org/10.1063/1.3480419.

[51] J. Ye, Shape anisotropy and instability of holes formed during de-wetting of single-crystal palladium and nickel films, J. Vac. Sci. Technol. A 33 (2015) 060601, http://dx.doi.org/10.1116/1.4926373.

[52] A. Gray, Modern Differential Geometry, 2nd ed., Chapman & Hall/CRC, Boca Raton, FL 2006, p. 269 (Chapter 13).

[53] O.D. Kellogg, Foundations of Potential Theory, Dover Publishing Inc., New York 1954, pp. 84–88.

[54] J.L. Synge, A. Schild, Tensor Calculus, University of Toronto Press, Toronto, Canada 1949, p. 194.

[55] M.E. Glicksman, Principles of Solidification (Chapter 4), Springer, USA, New-York 2011, pp. 69–97.

[56] G. Arfken, Mathematical Methods for Physicists (Chapter 1), 3rd ed., Academic Press, Orlando, FL 1985, pp. 1–84.

[57] J.S. Langer, Instabilities and pattern formation in crystal growth, Rev. Mod. Phys. 52 (1980) 1–28.

[58] K. Kassner, Pattern Formation in Diffusion-Limited Crystal Growth, World Scientific Publishing Co. Pte. Ltd., Singapore 1996, pp. 245–246.

[59] E. Gamsjäger, J. Svoboda, F.D. Fischer, M. Rettenmayr, Kinetics of solute driven melting solidification, Acta. Mater. 55 (2007) 2599–2607.

[60] M. Rettenmayr, M. Buchmann, Modeling rapid liquid/solid and solid/liquid phase transformation in Al alloys, Int. J. Mater. Res. 99 (2008) 613.

[61] G.J. McFadden, Private communication NIST, Gaithersburg, MD, 2006.

[62] A. Karma, Fluctuations in solidification, Phys. Rev. E 48 (1993) 3441–3458.

[63] A. Karma, Erratum: fluctuations in solidification, Phys. Rev. E 49 (1994) 3547.

[64] M. Glicksman, J. Lowengrub, S. Li, Non-monotone temperature boundary conditions in dendritic growth, in: C.A. Gandin, M. Bellet (Eds.), Modelling of Casting, Welding and Advanced Solidification Processes XI, TMS, Warrendale, MI, 2006, pp. 521–527.

[65] A.M. Mullis, Private communication University of Leeds, U.K., 2014.

[66] A.M. Mullis, Spontaneous deterministic side-branching behavior in phase-field simulations of equiaxed dendritic growth, J. Appl. Phys. 117 (2015) 114305, http://dx.doi.org/10.1063/1.4915278.

[67] S. Li, J. Lowengrub, P. Leo, V. Cristini, Nonlinear theory of self-similar crystal growth and melting, J. Cryst. Growth 267 (2004) 703–713.

[68] S. Li, J. Lowengrub, P. Leo, V. Cristini, Nonlinear stability analysis of self-similar crystal growth: control of the Mullins–Sekerka instability, J. Cryst. Growth 277 (2005) 578–592.

[69] S. Li, J. Lowengrub, P. Leo, A rescaling scheme with application to the long-time simulation of viscous fingering in a Hele-Shaw cell, J. Comp. Phys. 225 (2007) 554–557.

[70] M.E. Glicksman, J. Lowengrub, S. Li, Deterministic mechanism for dendritic solidification kinetics, J. Met. 59 (2007) 27–34.

[71] K. Reuther, M. Rettenmayr, Simulating phase transformations by a meshless method with front tracking, Acta Mater. 60 (2012) 2128–2134.

[72] K. Reuther, M. Rettenmayr, Simulating dendritic solidification using an anisotropy-free meshless front-tracking method, J. Comp. Phys. 279 (2014) 63–66.

[73] H. Carslaw, J. Jaeger, Conduction of Heat in Solids, 2nd ed., Clarendon Press, Oxford, 1959.

[74] J. Crank, The Mathematics of Diffusion, 2nd ed., Clarendon Press, Oxford, 1995.

[75] V. Alexiades, A.D. Solomon, Mathematical Modeling of Melting and Freezing Processes, Hemisphere Publishing Corp, Washington, DC 1993, pp. 93–94 (Chapter 2).

[76] J. Lowengrub, University of California, Irvine, CA, S. Li, Illinois Institute of Technology, Chicago, IL, Simulations of equiaxed dendritic growth, Private communications, 2011, 2012.

[77] K. Ankit, B. Nestler, Institute of Applied Materials–Computational Materials Science, Karlsruhe Institute of Technology, Karlsruhe, Germany, Private communication, 2015.

[78] A. Choudhury, B. Nestler, Grand-potential formulation for multicomponent phase transformations combined with thin-interface asymptotics of the double-obstacle potential, Phys. Rev. E 85 (2012) 021602.

[79] M. Plapp, Unified derivation of phase-field models for alloy solidification from a grand-potential functional, Phys. Rev. E 84 (2011) 031601.

[80] P.G. Saffman, G.I. Taylor, The penetration of a fluid into a porous medium of Hele-Shaw cell containing a more viscous liquid, Proc. R. Soc. Lond. A 245 (1958) 312–329.

[81] R. Trivedi, S. Liu, S. Williams, Interface pattern formation in nonlinear dissipative systems, Nat. Mater. 1 (2002) 157–159.

[82] J.-X. You, Z.-J. Wang, J.-J. Li, J.-C. Wang, Tip-splitting instability in directional solidification based on bias field method, Chin. Phys. B 24 (7) (2015) 78–107.

[83] B.N. Flanders, Directed electrochemical nanowire assembly: precise nanostructure assembly via dendritic solidification, Mod. Phys. Lett. B 26 (2012) 113001, http://dx.doi.org/10.1142/S0217984911300018 (33 pp.).